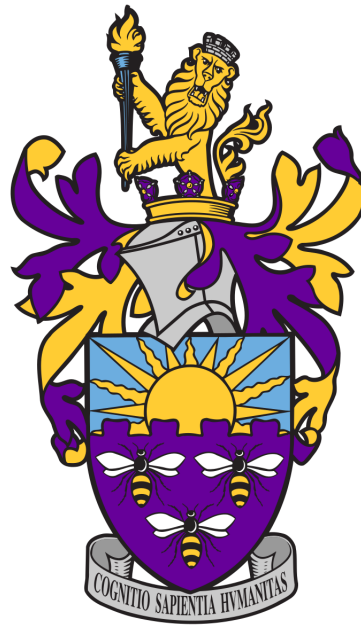


Development of a probabilistic method to extract double pomeron exchange events in high pile-up conditions with the AFP detector



A DISSERTATION SUBMITTED TO THE UNIVERSITY OF MANCHESTER
FOR THE DEGREE OF MASTER OF SCIENCE BY RESEARCH OF PARTICLE PHYSICS
IN THE FACULTY OF SCIENCE AND ENGINEERING

Huazhen Li

School of Natural Sciences
Department of Physics and Astronomy

2022

Contents

List of figures	3
List of tables	6
1 Introduction	1
2 Theoretical Background	3
2.1 Standard Model	3
2.2 Proton-proton Interactions	5
2.3 Kinematics of Elastic and Diffractive Processes	9
2.4 Status of Diffraction at the LHC	12
2.5 Photon Fusion Processes	13
3 Detectors	14
3.1 The LHC	14
3.1.1 Structure of the LHC	14
3.1.2 Proton Beam Structure	16
3.1.3 Average Number of Interaction Per Bunch Crossing	17
3.2 The ATLAS Experiment	18
3.2.1 The Main Structure of the ATLAS Detector	18
3.2.2 ATLAS Trigger System	20
3.3 The ATLAS Forward Proton Sub-detector	21
3.3.1 Mechanics of Roman Pot	22
3.3.2 The AFP Silicon Tracker	22
3.3.3 The Time-of-Flight Detector (ToF)	24
3.3.4 The AFP Performance in 2017	25
4 Development of a Probabilistic Model and Simulation	27
4.1 Definitions	28

4.2	Deriving Expressions for a Bunch Crossing with Fixed Number of Proton-proton Interactions	29
4.3	Cancellation of Actual Number of Proton-proton Interactions Per Bunch Crossing	31
4.4	Deductions from the Probabilistic Model	32
4.5	Emulation of the Probabilistic Model	33
5	Data Analysis	39
5.1	Event Selection	39
5.1.1	ATLAS Trigger Menu	39
5.1.2	Good Run List (GRL)	40
5.1.3	Proton Selection	42
5.2	Results of Data Analysis	43
5.2.1	Distributions of Physical Quantities and Performance of the AFP	43
5.2.2	Event Mixing	47
5.2.3	Application of the Probabilistic Model in Data	49
5.3	Conclusion	55
	References	57

List of figures

2.1	Feynman diagram of non-diffractive process in proton-proton interactions on LHC.	6
2.2	Feynman diagrams of elastic and diffractive processes in proton-proton interactions on LHC.	7
2.3	Plots of proton-proton elastic cross section from multiple experiments.	8
2.4	Differential cross section as a function of M_X^2/s of proton-proton single diffraction process, which is related to ζ	11
2.5	Total, elastic and inelastic cross section as functions of center-of-mass energy on LHC from multiple experiments.	12
2.6	Feynman diagram of photon fusion process with single particle produce from the $\gamma - \gamma$ system.	13
3.1	The Beam Structure of CERN Accelerator Complex.	15
3.2	Schematic plot of LHC storage ring cross section.	16
3.3	The integrated luminosity of ATLAS run 2 measurement in 2017 (left) and mean number of interaction per bunch crossing measurements in each year from 2015 to 2017 (right)	17
3.4	Schematic plot of ATLAS	20
3.5	Schematic plot of AFP	21
3.6	Geometrical structure of the Roman pot.	22
3.7	Time-of-Flight detector and the geometry of L-shape cherenkov radiator.	24

3.8	2D histogram of AFP acceptance as a function of relative energy loss ξ and proton transverse momentum p_T	26
3.9	Efficiencies of 4 AFP stations in different runs in 2017.	26
4.1	Flow chart of the simulator program.	34
4.2	Comparisons between input probabilities and output probabilities from the simulator.	35
4.3	Output probabilities as functions of μ values when detecting efficiencies $\varepsilon \neq 1$ are involved, together with their linear fit curves.	36
4.4	Comparison between the input probabilities and corresponding output probabilities, together with the comparison between the output P_{AC} and input event number.	37
4.5	Plots of output probabilities as functions of ε values when other probabilities are constant.	38
5.1	A list of some typical triggers in the primary physics trigger menu and their trigger rates.	41
5.2	The distribution of average proton-proton interactions number per bunch crossing.	44
5.3	The number of protons reconstructed on each side of AFP.	45
5.4	The distributions of ξ_A (left) and ξ_C (right) for events with only one proton detected on both A-side and C-side.	46
5.5	Missing mass distribution of events with only one proton detected on both A-side and C-side.	47
5.6	The schematic plot of event mixing procedure.	48
5.7	The distribution of missing mass as well as the distribution of manually produced "mixed" missing mass, with is drawn in logarithm scale. The normalised missing mass distribution from "mixed" events is presented as the markers, and the rigid line histogram represents the missing mass distribution from "normal" events.	48

5.8	Calculated four underlying probabilities as functions of average proton-proton interaction number per bunch crossing. A linear fitting is also applied for each of them, showing non-zero gradients for the probabilities.	50
5.9	Relative differences of underlying probabilities after μ is shifted by an absolute value. Two optional values for the shifting are considered. . .	51
5.10	Relative differences of underlying probabilities after μ is shifted slightly by a small fraction. Two optional relative values for the shifting are considered.	52
5.11	P_A calculated using data from different runs, drawn with respect to μ , together with a the efficiencies of 4 AFP stations in different runs. The coloured arrows point out the time positions of the runs.	53
5.12	P_C and P_{AC} calculated using data from different runs, drawn with respect to μ	54

List of tables

2.1 Elementary particles introduced in the standard model and their electric charge and spin/parity. 4

Abstract

ATLAS is a multi-purpose spectrometer taking data at 14 TeV LHC accelerator at CERN since 2007. The ATLAS Forward Proton (the AFP) sub-detector is an important upgrade to the ATLAS detector which promises an extension to the physics reach of ATLAS. In this research, a probabilistic method using predefined underlying probabilities is established to describe the diffractive proton-proton interactions in ATLAS, and then using 1.22×10^9 events collected on the AFP detector in 2017, the underlying probabilities are measured to be

$$\begin{aligned}P_A &= (14.0 \pm 0.001) \times 10^{-3}, \\P_C &= (14.4 \pm 0.001) \times 10^{-3}, \\P_{AC} &= (2.0 \pm 0.008) \times 10^{-4}, \\P_0 &= (969.6 \pm 0.003) \times 10^{-3}.\end{aligned}$$

from which the latest experimental result of Double Pomeron Exchange (DPE) process (e.g. the DPE cross section) on ATLAS can be extracted. In addition, the probabilities are found to be dependent on the average number of interactions per bunch crossing, and three possible causes are analysed.

Declaration

That no portion of the work referred to in the thesis has been submitted in support of an application for another degree or qualification of this or any other university or other institute of learning.

Huazhen Li

Copyright

- i. The author of this thesis (including any appendices and/or schedules to this thesis) owns certain copyright or related rights in it (the “Copyright”) and s/he has given The University of Manchester certain rights to use such Copyright, including for administrative purposes.
- ii. Copies of this thesis, either in full or in extracts and whether in hard or electronic copy, may be made **only** in accordance with the Copyright, Designs and Patents Act 1988 (as amended) and regulations issued under it or, where appropriate, in accordance with licensing agreements which the University has from time to time. This page must form part of any such copies made.
- iii. The ownership of certain Copyright, patents, designs, trade marks and other intellectual property (the “Intellectual Property”) and any reproductions of copyright works in the thesis, for example graphs and tables (“Reproductions”), which may be described in this thesis, may not be owned by the author and may be owned by third parties. Such Intellectual Property and Reproductions cannot and must not be made available for use without the prior written permission of the owner(s) of the relevant Intellectual Property and/or Reproductions.
- iv. Further information on the conditions under which disclosure, publication and commercialisation of this thesis, the Copyright and any Intellectual Property and/or Reproductions described in it may take place is available in the University IP Policy (see <http://documents.manchester.ac.uk/DocuInfo.aspx?DocID=24420>), in any relevant Thesis restriction declarations deposited in the University Library, The University Library’s regulations (see <http://www.library.manchester.ac.uk/about/regulations/>) and in The University’s policy on presentation of Theses.

Acknowledgements

I can not express enough thanks to the help of my supervisory team, Prof. Pilkington and Prof. Price. In the past year, an analytical research about ATLAS/AFP detector was conducted, and this research can never be finished without their kind and patient instruction. They helped me so much on learning how to conduct research works and they encouraged me to investigate the problem, finding the conclusion myself, which is really beneficial to my future research career in particle physics.

Besides, special thanks to the help of Savannah. As a senior PhD student specialised in the AFP detector, she helped me a lot on introducing the software to me, and helping me out of the analysis problems. Especially when I was confused about the structure of AFP data set, she explained everything clearly and patiently to me, which is really helpful.

Finally, thanks to my family and my friends, Lanxing, Zuchen and Zihan, they supported my life and helped me a lot in my study in the past year.

Word count: 9703

Chapter 1

Introduction

In 1974, the widely accepted theoretical description of Double Pomeron Exchange (DPE) process was established by D. Chew, G. Chew [1], and Shankar [2] using the framework of Triple-Regge theory [3]. Here DPE, or central diffraction, refers to the hadron-hadron process where a central diffractive system is produced (see Chapter 2). The experimental investigation about DPE processes initiated in 1969 at the Brookhaven 80" bubble chamber where interactions between pions and protons at a center of mass energy of 6.9 GeV were exploited. However, no clear evidence of the DPE process was observed, so the upper limit on the cross section of DPE in this experiment was measured to be $44 \mu b$. In following measurements, the upper limit was updated to $20 \mu b$ [4–7].

Then from 1971, at the CERN Intersecting Storage Rings (ISR), proton-proton interactions at a center-of-mass energy of 45 GeV were used. With the ISR data fit to a Triple Regge model, the existence of the process $\mathbb{P} + \mathbb{P} \rightarrow X$ was predicted, where \mathbb{P} is the pomeron, and X refers to any final states [6].

Finally in 1976, the first DPE process was observed by the Split Field Magnet (SFM) facility at ISR [5]. Then in following fixed-target experiments, for example E690 at the Fermilab Tevatron [8], it was confirmed that the existence of $\mathbb{P} + \mathbb{R}$ background (\mathbb{R} refers to the Reggeon) calls for the experiment using colliding beams. Therefore in following experiments like CDF [9] and CMS/TOTEM, DPE process was further investigated, and some of its characteristics, including the resonance structure shown in the spectrum of momentum transfer ($|t|$), and the cross section of DPE was measured. However, at the LHC, the DPE process has not been fully investigated on the ATLAS experiment yet. Especially after the installment of the AFP detector, the measurement of DPE cross section exploiting ATLAS/AFP detectors is of high significance.

In this research, we tried to establish a set of probabilistic models describing the proton-proton interactions in LHC and observed events in AFP, by which the cross section of DPE process in LHC can be indicated, and the performance of AFP detector can also be tested.

Apart from the introduction, this thesis can be divided into four chapters. In Chapter 2, the theoretical background of the AFP experiment, including the Standard Model and the proton-proton interaction in LHC is discussed. In Chapter 3, the structure of the LHC, ATLAS detector and AFP sub-detector is introduced, in which the detecting process of the detectors is also introduced. Then Chapter 4 establishes a probabilistic model based on the theory introduced in Chapter 2 and predefined underlying probabilities. Then a simulation of the toy model is used to show the expected results of the underlying probabilities. Finally, in Chapter 5, the results of the data analysis, together with the description of the data set we used is displayed. The performance of AFP in multiple measurements, as well as the analysis of underlying probabilities is shown.

Chapter 2

Theoretical Background

2.1 Standard Model

The Standard Model (SM) of particle physics is a quantum field theory that successfully describes all of the fundamental particles and their interactions. This theory is mathematically based on the unitary product group $SU(3)_C \times SU(2)_L \times U(1)_Y$. The $SU(3)_C$ group describes the interaction mediated by the strong force (quantum chromodynamics, QCD), and the $SU(2)_L \times U(1)_Y$ describe the unification of weak and electromagnetic interaction between particles.

The elementary particles introduced in the SM are listed in table 2.1 [10]. In the SM, three fundamental interactions are mediated by spin-1 gauge bosons. The strong force is mediated by the gluon (g). The weak force is mediated by the W and Z bosons. The electromagnetic force is mediated by the photon (γ). However, the gravitational interaction can not be described by SM, but it can be neglected here for it is significantly weaker compared with other interactions between particles [11–13].

Fermions are the spin- $\frac{1}{2}$ particles that make up matter, and they can be further divided into quarks and leptons. Leptons are elementary particles including electron (e^-), muon (μ^-), tau lepton (τ^-), and their corresponding three neutrinos, ν_e , ν_μ and ν_τ . Quarks, which consists of six members: u , c , t , d , s and b , can form bound states called hadrons with the strong interaction carried by gluons. Quarks can interact through strong forces, and they can also have electromagnetic interaction with other charged particles. Besides, quarks can also have weak interactions with other quarks or leptons. As for leptons, charged leptons (electron, muon and tau lepton) can have

Particle Type	Sub-type	Name	J^P	Electric Charge
boson	gauge boson	γ	1^-	0
		g	1^-	0
		W	$J = 1$	± 1
		Z	$J = 1$	0
		H^0	$J = 0$	0
fermion	quark	u	$1/2^+$	+2/3
		c		+2/3
		t		+2/3
		d		-1/3
		s		-1/3
		b		-1/3
	lepton	e	$J = 1/2$	-1
		μ		-1
		τ		-1
		ν_e		0
		ν_μ		0
		ν_τ		0

Table 2.1: Elementary particles introduced in the standard model and their electric charge and spin/parity [10].

electromagnetic interactions with charged particles and weak interactions with other leptons or quarks, and neutrinos can have weak interactions with other particles.

Another special boson introduced in the SM is the Higgs boson. It is a spin-0 boson introduced to explain the origin of particle mass [14]. In the SM, gauge bosons acquire masses by spontaneous symmetry breaking of the Higgs field, and fermion masses come from their interactions with the Higgs field [15, 16]. However the neutrino mass, as a lone exception, is zero in the SM, for neutrinos are all left handed, providing no contribution to the neutrino mass term in the Yukawa coupling [17].

In QCD, by analogy with the electrical charge introduced to describe the electromagnetic interaction, the strong interactions between quarks and gluons are described in terms of a property of particles called "colour charge". Each of the six quarks can carry one of the three positive colour charges: red, blue and green, and each of the six anti-quarks can carry one of the three negative colour charges: antired, antiblue and

antigreen. Any colour charge can annihilate with its corresponding opposite colour charge, and a particle carrying all of the three positive colour charges has a net colour charge of zero. Moreover, gluon can carry two colour charges: one colour charge and one opposite colour charge, and the net colour charge of a gluon can not be zero (which means the colour configuration like red-antired is not permitted for gluons). Therefore, there are in total eight colour configurations for gluons forming an octet: $r\bar{b}$, $r\bar{g}$, $g\bar{b}$, $g\bar{r}$, $b\bar{r}$, $g\bar{g}$, $\frac{1}{\sqrt{2}}(r\bar{r} - g\bar{g})$, and $\frac{1}{\sqrt{6}}(r\bar{r} + g\bar{g} - 2b\bar{b})$.

According to QCD, only those particles with zero net colour charge can be observed as independent states, which explains why we can not observe independent quarks or gluons. This is called the colour confinement. As a result, we can only observe hadrons instead of quarks, and there are only three possible types of hadrons (except the special type of hadrons called glueballs, which do not contain quarks): baryons with three quarks, antibaryons with three antiquarks and mesons made up of one quark and one antiquark. The colour confinement comes from another feature of QCD called the asymptotic freedom, which refers to the feature that the strength of the strong interaction between quarks is asymptotically weaker as the energy scale increases. At low energies, however, the interaction between the quarks become stronger, which leads to the confinement [18].

2.2 Proton-proton Interactions

The proton-proton interactions can be divided into five types: single diffractive interactions, elastic scatterings, double diffractive interactions, double pomeron exchange processes and non-diffractive interactions [19,20].

Non-diffractive interactions involve coloured object exchange. The Feynman diagram of a specific non-diffractive process is shown in figure 2.1, which shows that the coloured object exchange will cause both interacting protons to dissociate into a number of different particles. Apart from the scattered protons, the exchanged coloured object could scatter to form final states with partons.

The other four interactions, however, only involve colour-less object exchange. Such strongly interacting object is called pomeron [19,21]. The Feynman diagrams of possible elastic and diffractive processes are shown in figure 2.2, in which the pomeron is represented by double lines.

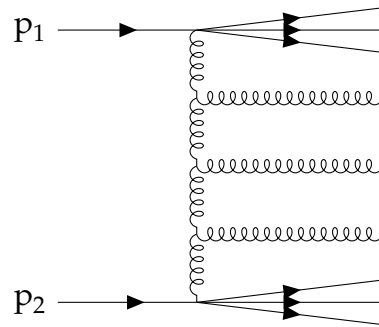


Figure 2.1: Feynman diagram of non-diffractive process in proton-proton interactions, in which the two interacting protons have a coloured object exchange, represented as helical lines in the diagram. After the interaction, both protons are scattered [19].

The first interaction shown in figure 2.2(a) is the elastic scattering process, in which both protons remain intact during the proton-proton interaction, with one pomeron exchanged between the two interacting protons, and there are no other final states produced.

The second process shown as figure 2.2(b) is called "single diffraction". In such processes, one of the two protons is scattered while the other one remains intact during the proton-proton interaction. On the scattered proton side, because of the confinement, a lot of hadrons will be produced instead of the original proton.

The third one in figure 2.2(c) is called "double diffraction", in which both two protons are scattered. Similar to the single diffraction, both protons are scattered in to groups of hadrons in this process.

In elastic and diffractive processes, it is possible that two pomerons emitted from both protons can have interactions. This process is called central diffraction, or, double pomeron exchange (DPE) process. A specific Feynman diagram of DPE is shown as figure 2.2(d). In DPE processes, apart from the two interacting protons, there are extra final states coming from the pomeron interaction.

In non-diffractive interaction processes, the particle production is mainly in the central and mid-rapidity region, while in elastic and diffractive processes the final states are concentrated in forward direction, because compared with non-diffractive interactions, the momentum exchange between the two protons in diffractive processes is relatively small. In elastic scatterings and single/double diffraction, the central rapidity region will be devoid of final state particles, which is called "the rapidity gap" [19,20].

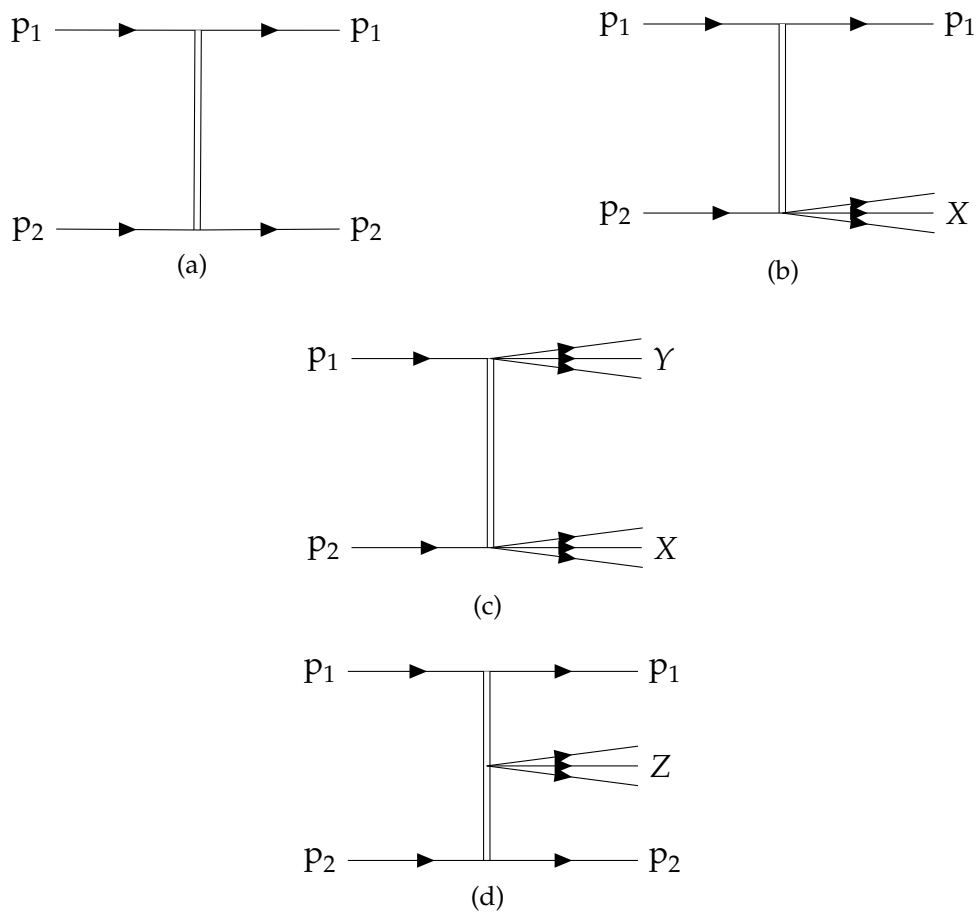


Figure 2.2: Feynman diagrams of elastic and diffractive processes in proton-proton interactions on LHC. Colour-less object (pomeron) exchange is involved in these processes, represented as double plain lines in the diagrams. (a) Elastic scattering, (b) single diffraction process, (c) double diffraction process, (d) double pomeron exchange process (central diffraction) [19].

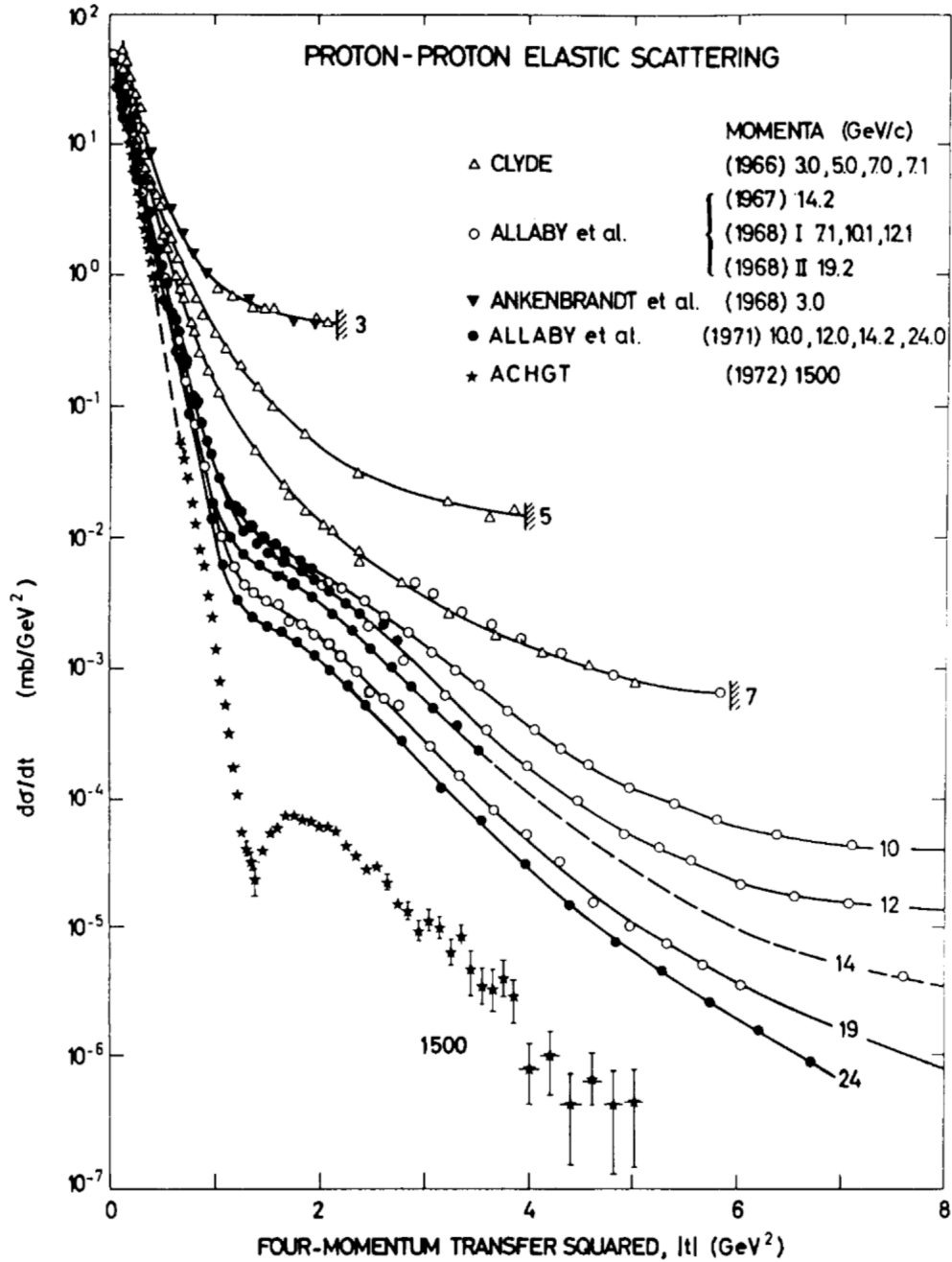


Figure 2.3: Plots of proton-proton elastic cross section from multiple experiments, with squared momentum transfer varied from 0 to 8 GeV² [22].

2.3 Kinematics of Elastic and Diffractive Processes

In this section, a set of kinematic variables are introduced to describe the elastic and diffractive processes which include elastic scattering, single diffraction, double diffraction and double pomeron exchange processes. These interactions have at least one intact forward proton in the final states.

First, we need to introduce the fractional momentum loss of intact proton, ξ , which is defined as:

$$\xi = \frac{\Delta \vec{p}}{\vec{p}} \approx 1 - \frac{E'_p}{E_p}, \quad (2.1)$$

where ξ can also be approximately written as the fractional energy loss in high energy proton-proton collisions. Other important kinematic variable are the squared energy of center of mass system s , and the four momentum transfer between the two interacting protons, $|t|$, defined as

$$|t| = |p_{p'} - p_p|, \quad (2.2)$$

in which p_p and $p_{p'}$ are separately the momentum of the initial and final state of the intact proton in the interaction.

In an elastic scattering process, ξ is defined to be zero because of the momentum conservation, but it has a non-zero t -structure [22]. As is shown in figure 2.3, according to various experimental results, the differential cross section of proton-proton interaction, $\frac{d\sigma}{dt}$, has the maximum value at $t = 0$, but it has a continuous distribution in non-zero region. As energy increases, the effect of diffraction can be identified. In diffractive processes, however, $\xi \neq 0$ for the collision leads to the dissociation of proton and the process is no longer elastic.

In theory, the cross section of diffractive processes is described by Regge phenomenology [23]. With Mullers generalisation of the optical theorem [24] applied when the center of mass energy \sqrt{s} satisfies $s \gg M_X \gg M_p$, the cross section of single diffractive process can be expressed [21] by

$$\frac{d^2\sigma}{d\xi dt} = \left(\frac{1}{\xi}\right)^{2\alpha(t)-1} \left(M_X^2\right)^{\alpha(0)-1} e^{B_0 t}, \quad (2.3)$$

in which M_X represents the invariant mass of the diffractive system X of the dissociated proton. M_p is the proton mass, $\alpha(0)$ is the intercept of the proton trajectory, $\alpha(t)$, and B_0 is the empirical parameter characterising the spatial size of scattering protons. Therefore at fixed s and M_X , the differential cross section can be written with an exponential relationship with t as follows:

$$\frac{d\sigma}{dt} \propto e^{B(M_X^2, s)t}, \quad (2.4)$$

where B is the slope factor absorbing other parameters by $B = B_0 - 2\alpha' \ln \zeta$, and α' is the slope of pomeron trajectory. Integrated over t between the lower limit t_{low} and upper limit t_{up} , the differential cross section as a function of ζ can be derived as

$$\frac{d\sigma}{d\zeta} = \left(\frac{1}{\zeta}\right)^{\alpha(0)} \frac{e^{Bt_{up}} - e^{Bt_{low}}}{B}, \quad (2.5)$$

which shows that the differential cross section measurement is equivalent to the measurement of intercept $\alpha(0)$, and the differential cross section is a negative power function of ζ .

For single diffraction, there exists a kinematic relationship [21] between the invariant mass of the dissociated proton, M_X , and the fractional momentum loss of the intact proton, ζ :

$$\zeta = \frac{M_X^2}{s}. \quad (2.6)$$

In experiments, measuring the invariant mass M_X directly is usually not practical, for the acceptance of detectors is limited. Thus, the measurement of fractional momentum loss ζ is commonly used to obtain the M_X . Moreover, the differential cross section acts differently in different regions of the M_X . In high mass region, the differential cross section follows the $1/M_X^2$ decrease, and forms a continuum. However in the low mass region, a resonance-like structure imposed on the continuum exists. This is shown as figure 2.4 [22].

Similar to single diffraction, fractional momentum loss of the two intact protons in double pomeron exchange processes can be separately defined as ζ_1 and ζ_2 . There exists a kinematic relationship between the two fractions and the invariant mass of the dissociated system Z produced by the pomerons, M_Z , and the squared center of mass

energy, s :

$$\tilde{\zeta}_1 \tilde{\zeta}_2 = \frac{M_Z^2}{s}, \quad (2.7)$$

which also shows that the measurement of invariant mass M_Z is equivalent to the measurement of fractions $\tilde{\zeta}_1$ and $\tilde{\zeta}_2$.

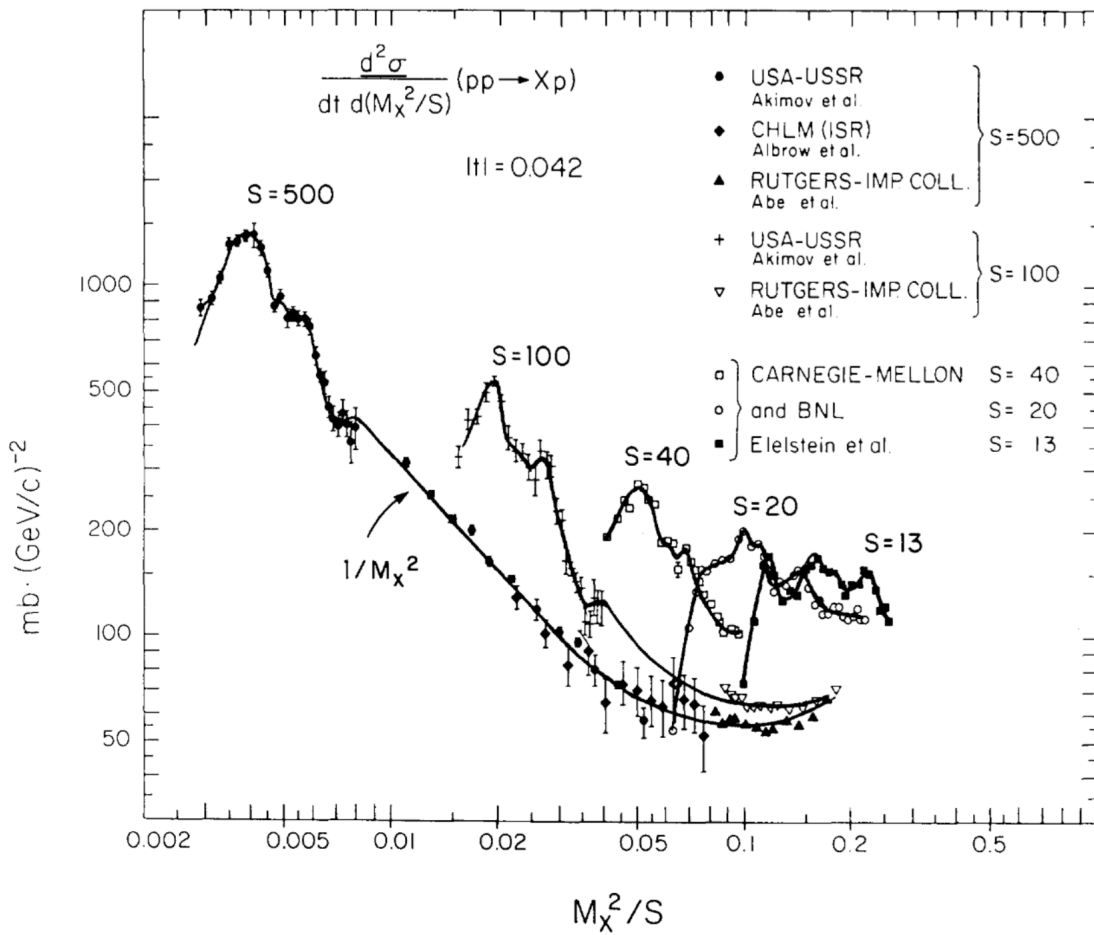


Figure 2.4: Plots of differential cross section as a function of M_X^2/s of proton-proton single diffraction process, which is related to ζ [22].

2.4 Status of Diffraction at the LHC

At the LHC, different strategies are exploited by different experiments to investigate the forward protons and diffraction. For example, the LHCb and ALICE experiments use the rapidity gap to select the diffractive events, while the ATLAS and CMS experiments use forward physics detectors, like ATLAS/ALFA, ATLAS/AFP and CMS/TOTEM to investigate diffraction [25].

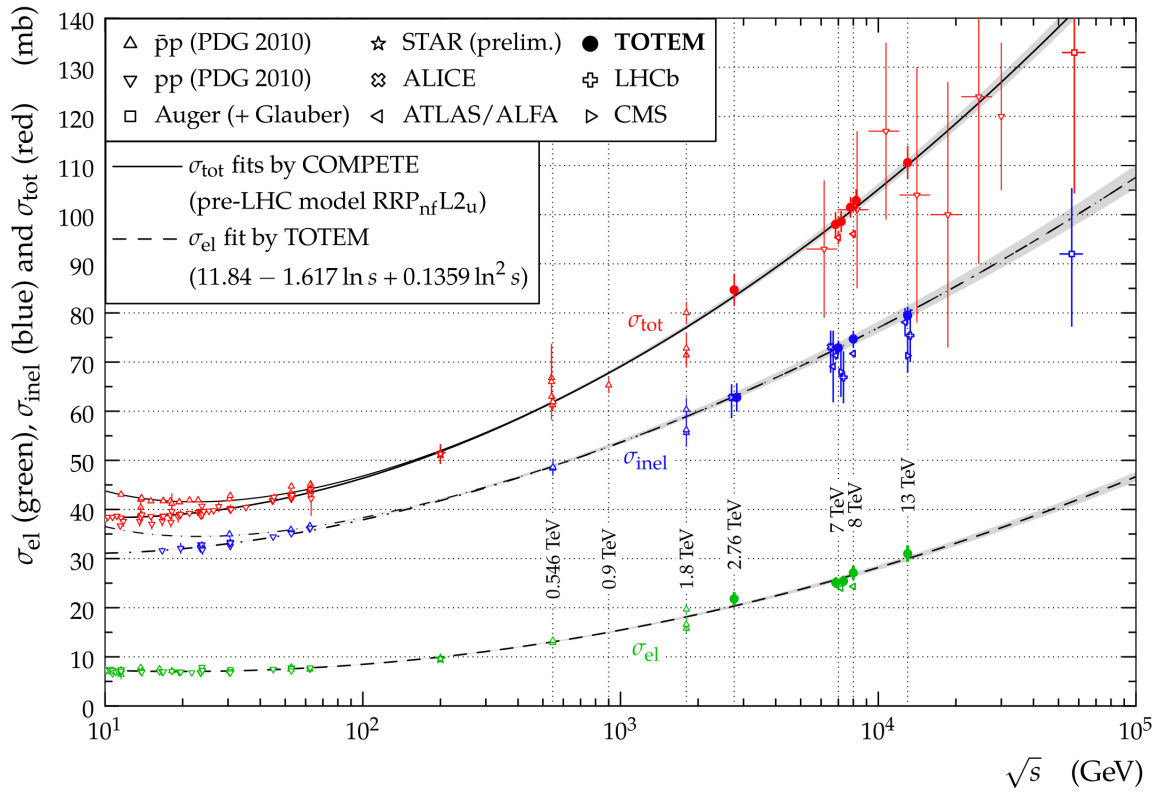


Figure 2.5: Total (red), elastic (green) and inelastic (blue) cross section as functions of center-of-mass energy from multiple experiments at the LHC [26].

For elastic scatterings, the elastic, inelastic and total cross sections as functions of center of mass energy are shown in figure 2.5, which shows results from multiple experiments, including ATLAS, CMS, LHCb and ALICE [26]. All of the three cross sections increase as the energy increases.

However, for diffractive cross sections, further to the early results from Fermilab, measurements at the LHC are much fewer, especially the diffractive process at ATLAS, and the cross section of double pomeron exchange process have not been measured. Therefore in this research, the double pomeron exchange process is investigated

by establishing a probabilistic model and experimentally analysing the introduced underlying probabilistic parameters.

2.5 Photon Fusion Processes

Photon fusion refers to a special DPE process that has a photon exchange between the two protons, and the photon-photon interaction could lead to various final states, for example, lepton anti-lepton pairs [27]. Among various photon fusion processes there is a special type, in which the two photons fuse into a single resonance. The Feynman diagram of this process is shown in figure 2.6. This special diagram is called axion-like particle signature, which can be used for dark matter searching at the LHC. If axion dark matter exists [28], one could expect the existence of process " $\gamma\gamma \rightarrow X$ ", in which X refers to a single particle.

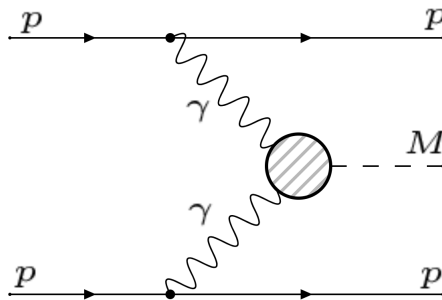


Figure 2.6: Feynman diagram of photon fusion process with single particle produce from the two photon system. The mass of the single particle is represented as M .

Now according to the figure 2.6, if we can get the invariant mass spectrum of the final states that come from the two photons' interaction, the searching for this process can be applied by checking if a peak signal shows up in the spectrum.

Chapter 3

Detectors

3.1 The LHC

This research uses the Run 2 data collected by the AFP sub-detector of the ATLAS experiment at the Large Hadron Collider (LHC). Starting from 2010, the LHC has played an important role in experimental particle physics research, and has expanded many new frontiers in particle physics in the past 12 years [29–31]. With a center of mass energy up to 14 TeV and design luminosity of $10^{34} \text{ cm}^{-2} \text{ s}^{-1}$, LHC is still the largest and most powerful proton-proton collider all over the world nowadays.

The idea of building the LHC initiated in 1977, when the Large Electron Positron (LEP) collider was still under construction. It was suggested that the LEP tunnel could be used to build a hadron collider after the operation of LEP ends. The LHC project was approved by CERN in 1994, and the construction started in 1998. The construction took about 10 years, and the first collision with a center of mass energy of 7 TeV was achieved in March 2010. Since then, the LHC has gone through two operational runs and two long shutdown periods. In Run-I, the LHC ran at a center of mass energy of 7 TeV, and in Run-II, it ran at a center of mass energy of 13 TeV, and it will be running at 14 TeV in Run-III [32,33].

3.1.1 Structure of the LHC

LHC is one part of the CERN accelerator complex, the structure of which is shown in Figure 3.1 [29,30]. Particles are accelerated step by step in different parts of the

complex, and the LHC, as the last element of the whole accelerator chain, has the highest beam energy of up to 7 TeV.

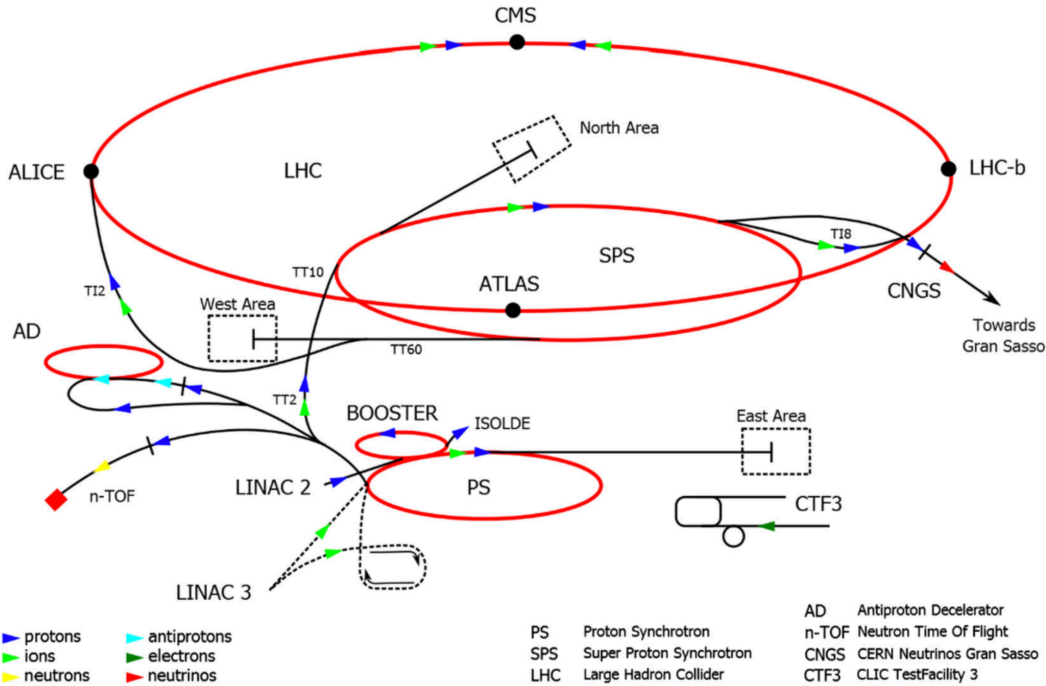


Figure 3.1: The Beam Structure of CERN Accelerator Complex. The LHC has the largest ring, also serves as the last element of the accelerator complex [29].

Two proton beams circulate in separate storage rings in opposite directions, and they have 4 colliding points, at which the four main detectors of LHC (ATLAS, LHCb, CMS, and ALICE) are located. Each ring is 26.7 km long, and they are both installed about 100 m below the surface. The cross-section view of the LHC dipole magnet is shown in Figure 3.2. The two rings are aligned horizontally, and are covered by a layer of cryogenic iron yoke, whose temperature is as low as 1.9 K. The low temperature is needed by the superconducting coils around each beam pipe, which are used to control the bending of proton beams through the magnetic field as strong as 8.3 T [31, 32].

The magnet system of the LHC consists of dipole magnets and quadrupole magnets. The dipole magnets are used for bending the proton beams, while the quadrupole magnets are used for focusing the proton beams. In total, there are 1232 main dipole magnets controlling 1232 bending points. 392 main quadrupole magnets on the arcs and other 148 main quadrupole magnets in the straight sections are installed to focus the beam [31, 32].

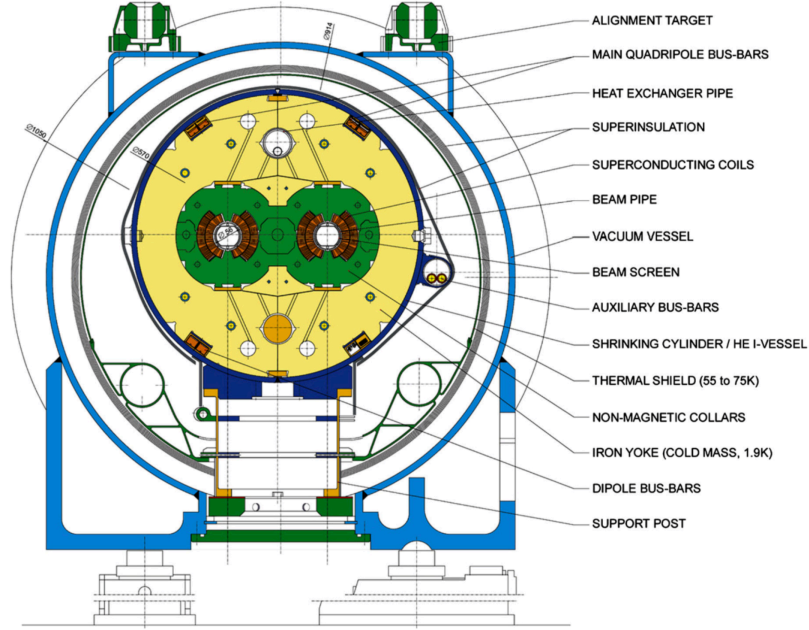


Figure 3.2: A typical cross section plot of LHC storage ring. The two beam pipes are hidden in dipole magnets that can produce a strong magnetic field of 8.3 T [29,30,34].

3.1.2 Proton Beam Structure

In each beam pipe, protons are stored in bunches. And bunches from the two beams collide in the 4 colliding points. The spatial and temporal structure of proton bunches are fixed. For example, the minimum distance between two bunches is 7.5 m (spatial distance) or 25 ns (temporal distance), and each beam holds at most 2808 proton bunches. These parameters can be used to calculate the instantaneous beam luminosity using the following expression [29,34].

$$L = \frac{kfN^2}{4\pi\sigma_x\sigma_y}, \quad (3.1a)$$

in which k stands for the number of bunches in the ring. f is the revolution frequency of the bunches, which is 11.24 kHz for the LHC. N is the number of protons in each bunch, which is up to 1.7×10^{11} . σ_x and σ_y are the typical sizes of bunches in x and y direction at interaction points, which are both about 20 μm [32].

On each interaction points, the two beams have a crossing angle to avoid unwanted collisions, which is important because of the high luminosity of the LHC. For high luminosity operations, a crossing angle of 285 μrad at each interaction point is planned.

3.1.3 Average Number of Interaction Per Bunch Crossing

With the instantaneous luminosity of the LHC obtained above, we can get the inelastic event rate [32,34]:

$$N_{tot}^{inel} = \sigma_{tot}^{inel} L, \quad (3.2)$$

in which the σ_{tot}^{inel} refers to the total inelastic cross section of proton-proton interaction. In the LHC, the high instantaneous luminosity condition leads to the result that the inelastic event rate N_{tot}^{inel} is large, and in each bunch crossing, the average inelastic event rate can be larger than one, from which the average number of interactions per bunch crossing (μ) can be defined as a function of instantaneous luminosity (L) as follows.

$$\mu = \frac{L\sigma_{tot}^{inel}}{kf_b}, \quad (3.3)$$

where k is the number of colliding bunches, f_b is the bunch crossing rate, and σ is the total inelastic cross section of the pp collision. The measurement result of integrated luminosity on ATLAS in 2017 and the corresponding average numbers of interactions per bunch crossing results are shown in Figure 3.3, from which we can conclude that in 2017, in LHC, about 50 fb^{-1} of data was delivered, and the average numbers of interactions per bunch crossing varies from 10 to 70 in 2017.

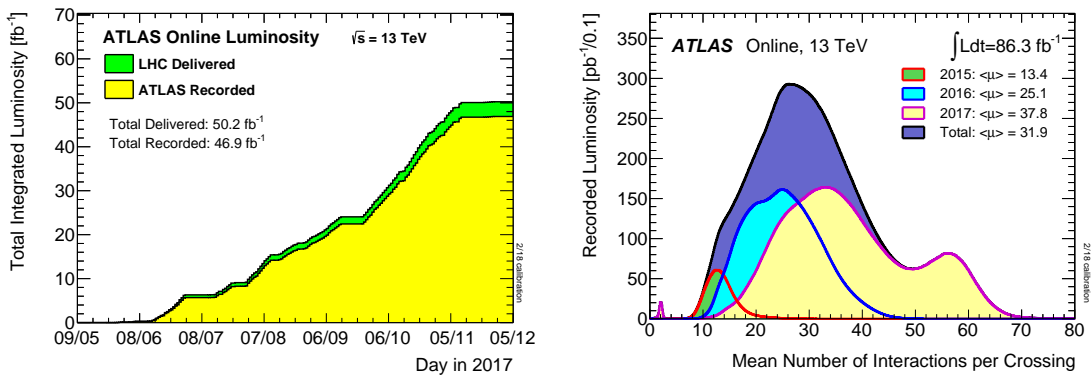


Figure 3.3: The integrated luminosity of ATLAS run 2 measurement in 2017 (left) and mean number of interaction per bunch crossing measurements in each year from 2015 to 2017 (right) [32].

3.2 The ATLAS Experiment

As a multi-purpose detector working on the LHC, the ATLAS (short for "A Toroidal LHC ApparatuS") experiment is designed for fully exploiting the discovery potential of the LHC. With a size of 46 m long, and 25 m in diameter, it has a nearly full coverage in solid angle, and a 2 T axial magnetic field produced by the superconducting solenoid and, a 3.5 T magnetic field generated by the toroidal magnet system [33]. The ATLAS detector is designed to obtain as many signatures as possible while operating under high luminosity conditions.

In this section, the structure and trigger system of ATLAS will be introduced, but definitions of the ATLAS coordinate system are needed. As is shown in figure 3.1, ATLAS is placed on one of four interaction points of LHC, so we can define a right-handed coordinate system as follows. The x axis direction is defined as the direction pointing to the center of the LHC tunnel, and y axis can be defined as the upward direction perpendicular to the ground. Therefore the z axis is fixed as the tangential direction of the LHC tunnel, and LHCb is on the +z side of ATLAS. Then we can name the +z side of ATLAS is the C-side, and the -z side of ATLAS is the A-side.

3.2.1 The Main Structure of the ATLAS Detector

As is shown in the ATLAS detector layout (Figure 3.4), the ATLAS detector is made up of three main sub-detector parts: inner detector (ID), electromagnetic (EM) and hadronic calorimeters, and muon spectrometer [33,35].

- **Inner detector**

The inner detector is placed in the center of ATLAS, inside the boundary defined by the calorimeter. The radius of the inner detector is 115 cm, and it has a length of 345 cm. It is enclosed in the solenoid, which provide the cavity with an axial central magnetic field of 2 T.

The inner detector consists of two main parts: Semiconductor Tracker (SCT), and Transition Radiation Tracker (TRT). The main purpose of them is measuring the direction, momentum, and electric charge of charged particles produced in the proton-proton interactions.

The SCT consists of pixel detectors and semiconductor strip detectors. Pixel detectors are used in the region nearest to the beam. The pixels are diodes made of silicon semiconductor and reversely connected to the high voltage power supply, so that a depletion area is formed. When a charged particle passes through a pixel detector on one of the layers, electron-hole pairs will be created through ionization, drifting toward the electrodes in the electric field, and creating a signal in the circuit, which can be recognised by front-end chips [36].

Semiconductor strip detectors are similar to pixels in principal, but each of them uses two single-sided semiconductor strip glued back to back perpendicularly to measure two coordinates separately.

At larger radii, TRT with firmly stacked straw tubes are used. With about 64 layers placed closely, more than 36 track points will be produced for each track, and they can be used for pattern recognition.

- **Calorimeter**

The calorimeter layer of ATLAS is placed outside the inner tracker cavity. The purpose of the calorimeters is measuring the energies of electrons, photons, and hadrons using energy depositions, and it consists of Liquid Argon (LAr) calorimeter and hadronic calorimeter.

The LAr calorimeter is closer to the beam, and it is used for measuring the energy of electrons, photons, and hadrons. It has two parts, heavy metal layers used for turning incident particles into electromagnetic showers, and the liquid argon in between the layers used for measuring the total energy of the showers by measuring the current caused by ionization.

The hadron calorimeter, which is placed outside the LAr calorimeter, uses plastic scintillating tiles to detect the energy of particles produced by showers in the steel plates.

- **Muon spectrometer**

In ATLAS, muons produced by proton-proton collisions usually pass through the inner detector and calorimeter undetected. Therefore using 4 different technologies: Thin Gap Chambers (TGC), Resistive Plate Chambers (RPC), Monitored Drift Tubes (MDT), and Cathode Strip Chambers (CSC), the muon detector is designed to measure the properties of muons as well as to be used for triggering.

In details, the TGC and RPC are used for triggering and measurement of the second coordinate. MDT is used for measuring the curve of the muon tracks, and CSC is designed for precise measurement of the coordinate.

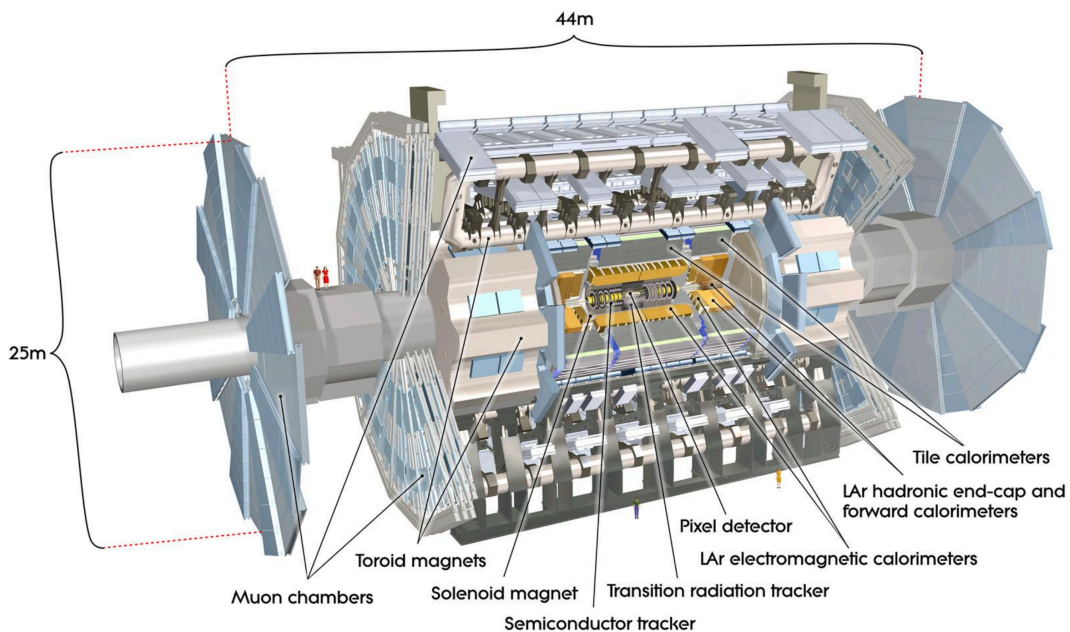


Figure 3.4: Layout view of ATLAS detector structure. ATLAS is a multi-purpose spectrometer that consists of 3 main sub-detector parts (ID, Calorimeter, and Muon Spectrometer) and Magnet system that consists of superconducting solenoid and toroidal magnets [35].

3.2.2 ATLAS Trigger System

Every second, interactions happen in the ATLAS detector at a rate of 40 MHz, which is far beyond the data processing ability of ATLAS. Therefore, a trigger system is needed to reduce the event rate, removing the trivial events, like, the events in which accelerated protons interact with the beam pipe, and the events that comes from cosmic rays going pass through the detector [33].

In ATLAS, there are two distinct trigger levels: L1 trigger, and High Level Trigger (HLT). The L1 trigger is the online hardware trigger that use the hit information on

different sub-detectors to make the selection. The HLT is a software-based trigger that uses reconstructed information to make the selection, which is referred to as online reconstruction. After the L1 and HLT, the event rates are reduced to roughly 1 kHz. This selected data is then transferred to the CERN Tier 0 computing center, for offline reconstruction and further data analysis. The whole collection of HLT triggers is called the "trigger menu".

3.3 The ATLAS Forward Proton Sub-detector

The ATLAS Forward Proton (AFP) sub-detector is designed to measure the four-momentum of forward protons produced in pp collisions at the ATLAS interaction point. The AFP detector therefore enables ATLAS to investigate the special events that contains intact protons, and the physics reach of ATLAS is expanded.

The AFP detector consists of four stations, with each station placed either at the NEAR point (205 m from the ATLAS interaction point) or at FAR point (217 m from the ATLAS IP) on each side. In each station, the detector consists of four layers of silicon tracker (SiT). For both FAR point stations, an additional Time-of-Flight (ToF) detector is placed behind the tracker. The layout of stations is shown in figure 3.5 [19,37].

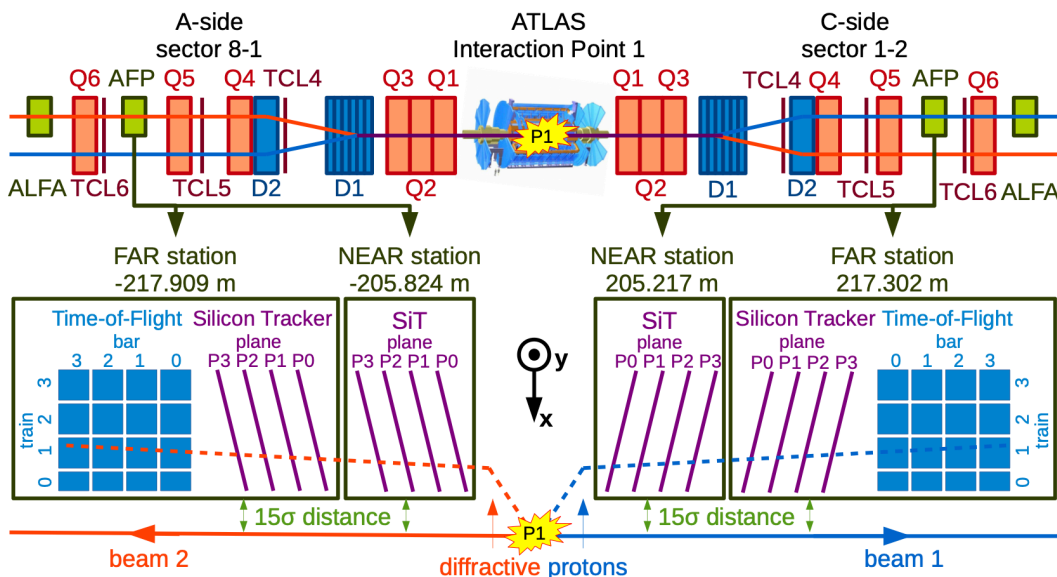


Figure 3.5: Schematic plot of AFP detector settings. Including the brief structure of Si trackers and ToF detectors in each station and their position on the beam line. [37, 38]

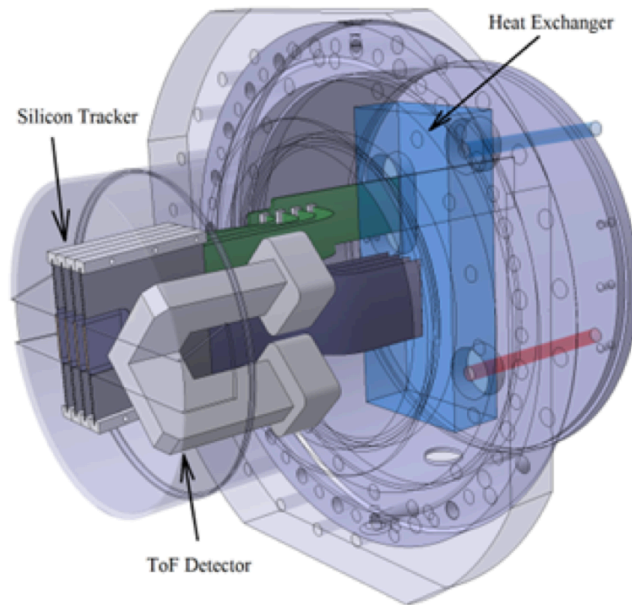


Figure 3.6: Geometrical structure of the Roman pot. This technical drawing shows the position and structure of SiT detectors and ToF detector. They are placed next to the beam. [19]

3.3.1 Mechanics of Roman Pot

Roman pot is the name for the steel vessels that hold the AFP detectors and protect the detector using a secondary vacuum. This technique was previously used on other forward proton experiments at the LHC like the ALFA and TOTEM detectors. As a detector that needs to be placed as close to the beam as possible, the AFP can easily be damaged by the proton beam when it is not stable during the injection [39].

Therefore, the roman pots are applied. As is shown in figure 3.6, the vessel is of cylindrical shape, and there is a thin window on it (left side of the AFP detector). Each roman pot is driven by a motor and it can move closer or further to the beam. During the injection, the pot is pulled away from the LHC beam. When the beam is stable, it can be pushed back in, and the trackers of AFP can be placed at several millimeters away from the beam.

3.3.2 The AFP Silicon Tracker

In order to provide a precise measurement of the scattered protons' momenta, four pixelated silicon tracking detector layers are installed in each station. The core com-

ponent of the tracking system is the pixel modules. Inside each module there is a 3D silicon sensor connected to a FE-I4B front-end chip and a flexible print chip. The whole module can provide 336×80 detecting pixels with a size of $50 \times 250 \mu\text{m}^2$. The total area of each module is $1.68 \times 2 \text{ cm}^2$, ensuring that the spatial resolution of the tracker could reach $\sigma_x = 10 \mu\text{m}$ in x direction, and $\sigma_y = 30 \mu\text{m}$ in y direction [19].

Similar to the silicon pixel detector used in the ATLAS inner tracker which is discussed above, when a charged particle passes through a pixel on an AFP tracker plane, ionised electrons and holes will be accelerated and create a signal in the circuit when they reach the columnar electrodes placed in the silicon base. Then the signal can be recognised by the front-end chips as a hit at corresponding pixel. Therefore, with multiple trackers working together, the tracks of charged particles can be reconstructed from hit patterns, from which the momentum of protons can be reconstructed.

In the SiT, the momentum reconstruction process of protons proceeds as follows. The χ^2 value of momentum can be calculated by measurement of hit position [19]:

$$\chi^2(\mathbf{p}) = \sum_i^{n_{station}} \left[\frac{(x_i^D - x_i(\mathbf{p}))^2}{\sigma_x^2} + \frac{(y_i^D - y_i(\mathbf{p}))^2}{\sigma_y^2} \right], \quad (3.4)$$

in which x_i^D and y_i^D stand for the coordinates of hit points on different stations. $x_i(\mathbf{p})$ and $y_i(\mathbf{p})$ are coordinate of points where proton trajectory goes pass through different stations. σ_x and σ_y are tracker resolution in x and y direction, and $n_{station}$ is the number of AFP stations which is four. By minimising the χ^2 , the momentum can be reconstructed. Then these geometrical parameters can provide the relative momentum loss of the protons ζ (defined as $\zeta = 1 - |\mathbf{p}_{proton}|/|\mathbf{p}_{beam}|$), meanwhile the four-momentum transfer squared t can be expressed by $\sqrt{|t|} = 2\sqrt{E_{proton}E_{beam}} \sin \theta/2$, where θ is the emission angle. Therefore the kinematic condition of protons can be fully determined.

Another constraint to the tracker system comes from the radiation hardness of the detector. The forward protons have a very small scattering angle, so the trackers are placed nearly perpendicular to the LHC beam. During data-taking, the tracker is only 2 to 3 mm from the beam, which requires the tracker to have an inactive area as small as $200 \mu\text{m}$ on the side that is facing the beam, and the trackers have to be able to withstand the highly non-uniform radiation condition of the beam.

3.3.3 The Time-of-Flight Detector (ToF)

The ToF detector of AFP is made up of two main parts. Quartz-Cherenkov Time-of-Flight Detector System, and multichannel plate photon-multiplier tube (MCP-PMT). It is designed to reduce the pile-up background events.

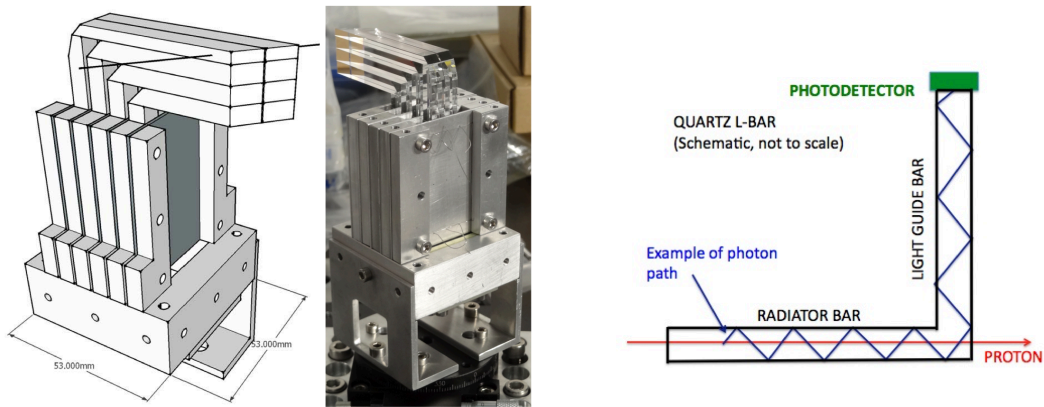


Figure 3.7: Time-of-Flight detector (left) and the geometry of L-shape Cherenkov radiator (right). [19, 40]

A picture of the Quartz-Cherenkov ToF detector, together with the geometry of each quartz crystal is shown in figure 3.7, which shows that the Quartz-Cherenkov ToF is made up of a series of straight high transparency quartz crystals serving as the Cherenkov radiator and wave guides that are attached to the crystals in a perpendicular angle [40]. In quartz crystals, when protons pass through, Cherenkov light is produced at an angle of $\theta_{ch} = \cos^{-1}(1/n\beta)$. Here n refers to the refractive index of quartz, and β is the relativistic velocity of protons. In the ToF, the radiator is placed at an angle of θ_{ch} with respect to the beam direction, so the Cherenkov light will penetrate the radiator in parallel with the direction of radiator bar, so that nearly all of the Cherenkov light will be trapped because of the total reflection of quartz. Then, through the wave guide, the Cherenkov light can be transferred to and detected by MCP-PMT. The MCP-PMT uses a photon cathode placed close to the quartz window to generate photo-electrons. Then avalanches can be generated in a ceramic plate on which there are pores parallel to a strong electric field. With an electric field of about 2.5 kV per plate, two plates could produce a gain of 10^6 . In order to reach the highest time resolution on the ToF, one practical method is having multiple measurements. Finally with the combination of multiple quartz crystal radiators and MCP-PMT, the ToF could reach a target time resolution of 10 ps [40].

For special low- μ runs, ToF is not essential, but for those standard luminosity runs, it is vital to use the time information from ToF. In order to separate the events of high interest, for example the DPE processes, and eliminate the pile-up events, ToF detectors separately placed on A-side and C-side are needed. For those process which we are interested in, two forward protons in the final states are produced at the same vertex, and the z -position of the vertex can be measured by measuring the difference between the time that each proton reach the AFP station, $\Delta t = |t_{left} - t_{right}|$. Therefore the measure of the z -position of the vertex is:

$$z_{vertex} = \frac{c\Delta t}{2}, \quad (3.5)$$

where c is the light velocity. The z_{vertex} measured by AFP should be correlated with the vertex position measured by ATLAS central detector. However, in those background events the two forward protons in final states comes from two single diffractive events which have two different vertices. There is no correlation between the z_{vertex} measured by AFP and the z_{vertex} got from the ATLAS central detector, so the background can be eliminated.

3.3.4 The AFP Performance in 2017

Figure 3.8 shows the AFP geometric acceptance as a function of relative energy loss ξ and transverse momentum p_T . A typical range of detected protons' energy loss is $0.025 < \xi < 0.1$. Secondly, figure 3.9 shows the efficiencies of 4 AFP stations for different runs in 2017. The efficiencies of NEAR stations are approximately 99%, while the FAR stations have efficiencies of approximately 95%, where the efficiency of the detector is defined as the probability of incident protons to be detected.

During 2017, the LHC delivered 49 fb^{-1} data, 97 % of which was recorded by ATLAS main detector, and 64 % of which was recorded by both ATLAS and AFP. So there are 32 fb^{-1} data recorded by AFP in 2017 in total. However, not all of the 32 fb^{-1} recorded data is usable. For example, some data was taken when the high voltage of all the AFP-SiT layers were off, and some were taken when the Roman pots of AFP stations were not inserted into the data taking position [19, 38].

Therefore, a series of selection criteria are needed for both ATLAS and AFP, making sure that the bad recorded events are eliminated. After the requirements are applied, the data will form a list of usable data called "good run list" (GRL), in which the AFP

data was reduced to 19.2 fb^{-1} , which will be introduced in details in following chapter 5 where the data we used for the analysis is described [38].

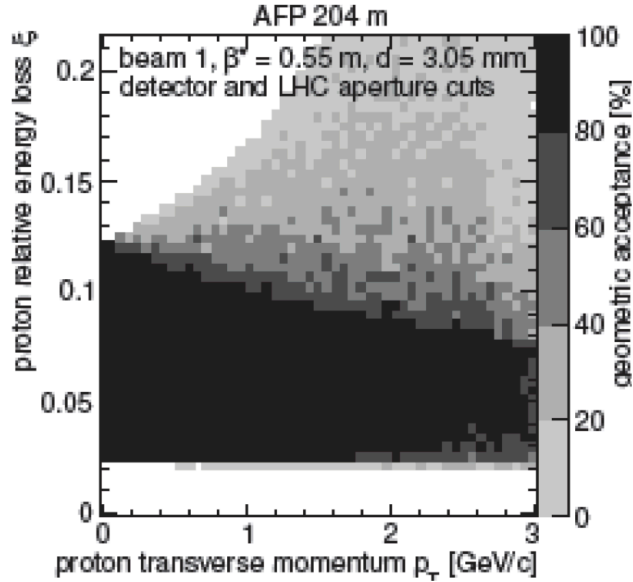


Figure 3.8: 2D histogram of AFP acceptance as a function of relative energy loss ξ and proton transverse momentum p_T . The typical range of ξ is from 0.025 to 0.1 when $p_T > 1 \text{ GeV}/c$, and the upper limit is higher for low p_T protons [19].

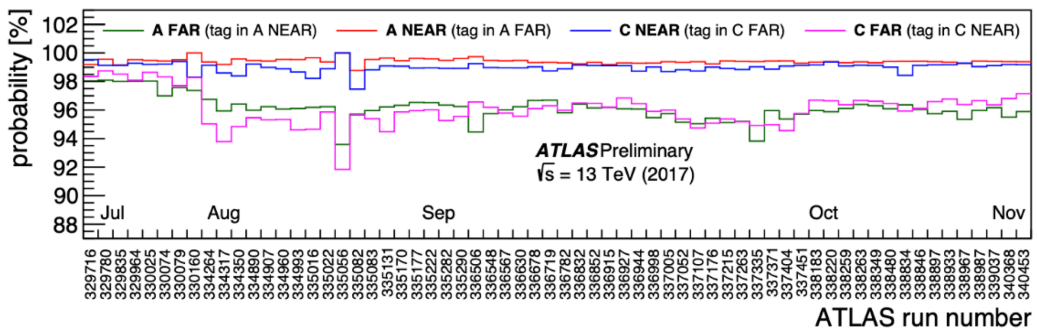


Figure 3.9: Efficiencies of 4 AFP stations in different runs in 2017. The efficiencies of NEAR stations are approximately 99%, while the FAR stations have efficiencies of approximately 95% [37].

Chapter 4

Development of a Probabilistic Model and Simulation

As is discussed in the first chapter, proton-proton interactions in the LHC include multiple interactions and this research mainly focus on DPE processes with two intact protons. Because of the existence of pile-up background events, the measurement of DPE processes in AFP data can not be directly given by counting the number of events which have one proton on each side in the final states. Furthermore, the pile-up events can not be separated from signal events using their difference in the missing mass spectral shape, either. Because no recognizable difference between the spectral shape of missing mass distribution from data events and background events that consist of proton tracks from different events shows up, which will be analysed in next chapter.

To test the properties of DPE processes $pp \rightarrow pXp$, we need to measure its cross section, $\sigma_{pp \rightarrow pXp}$, and differential cross section, $\frac{d\sigma_{pp \rightarrow pXp}}{dM_{miss}}$, at any given average number of proton-proton interactions per bunch crossing, μ . Ideally the cross section is related to the probability that one proton-proton interaction has two detected protons in the final states, P_{AC} , and the total inelastic cross section in proton-proton collisions, $\sigma_{inelastic}$ by following equation:

$$\sigma_{pp \rightarrow pXp} = \sigma_{inelastic} P_{AC}, \quad (4.1)$$

because under ideal circumstances P_{AC} is identical to the probability that one proton-proton interaction generates one proton on both A-side and C-side. However in actual world, things get complicated because of the existence of the detection efficiencies, ε_A

and ε_C , and it is possible that events with more than two protons in the final states be misjudged as the DPE events.

In this chapter, the definition and derivation of the probabilistic model is given, from which we can derive the expression of the number of bunch crossings that contain a known number of A-side and C-side protons written as functions of predefined probabilistic parameters.

In order to test the validity of the model, a simulator is written to simulate the bunch crossing condition in ATLAS. We first input a set of fixed parameters including the probabilities and average number of proton-proton interactions per bunch crossing, μ , and fixed detection efficiencies of A-side and C-side detectors, ε_A and ε_C , into the simulator. The simulator could simulate the proton-proton collision in ATLAS, and output a series of numbers of bunch crossings that contain known number of A-side and C-side protons. Then using the formalism established we can calculate the simulated values of probabilities. By comparing the simulation result and input values of probabilities, if the differences between the two sets of probabilities are relatively small compared with the input values, the correctness of the probabilistic model can be proved.

4.1 Definitions

According to the physics of proton-proton interactions at LHC and the proton detecting procedure of AFP detector [19], every single proton-proton interaction at ATLAS must have one of the four possible configurations: (1) only one proton detected on the A-side; (2) only one proton detected on the C-side; (3) one proton detected on each side; (4) no detected. Here we assume that for each proton-proton interaction, the probability of having any one of the configurations above is a constant, separately defined as P_A , P_C , P_{AC} and P_0 .

These probabilities are defined according to the number of protons **detected** on A-side or C-side detectors instead of the number of protons **produced** on A-side or C-side. The difference is coming from the detection efficiencies. For example, it is possible for a proton-proton interaction to produce one proton on both sides but only the proton on A-side is detected, and categorised as the configuration P_A . Therefore,

the definitions of these probabilities have already encapsulated the effect of detection efficiencies.

Another important parameter is the average number of proton-proton interactions per bunch crossing, μ . As is introduced in previous chapters, it is a parameter that characterises the severity of "pile-up" effect in a bunch crossing [19]. In the following derivations, the actual number of proton-proton interactions per bunch crossing, m , is also needed.

Apart from the parameters introduced above, we also need to define the number of bunch crossings that contain i observed A-side proton and j observed C-side protons, N_{ij} . The sum of N_{ij} over i and j should be the total number of bunch crossings, which is denoted as N_0 . The number of bunch crossings that contain m proton-proton interactions is defined as $N(m)$, the sum of which over m is also equal to N_0 .

4.2 Deriving Expressions for a Bunch Crossing with Fixed Number of Proton-proton Interactions

As discussed above, we need to establish a statistical relationship between the observed number of simultaneous proton signature (N_{ij}) detected on the A-side (i) and C-side (j) from a single proton bunch crossing, and the underlying probabilities of proton-proton interactions resulting in zero, one, or two forward protons as discussed in Section 3.1, as well as the expected number of proton-proton interactions in a single bunch crossing.

The first step of the derivation is to get the expression of N_{ij} as functions of the total number of proton-proton interactions, m , per given bunch crossing. The number of simultaneous proton signatures with m interactions, $N(m)$ can be described by the Poisson distribution as

$$N(m) = N_0 \mathcal{P}(\mu, m) = N_0 \frac{\mu^m}{m!} e^{-\mu}, \quad (4.2)$$

where $\mathcal{P}(\mu, m)$ is the normalised Poisson distribution function for m observed counts with a mean value of μ . Then we apply the separation of variables i and j on N_{ij} by

introducing a mathematical factor S_{ij} defined as the ratio of N_{ij} to $N(m)$, which means

$$N_{ij} = N(m)S_{ij}(m), \quad (4.3)$$

where $S_{ij}(m)$ is a function describing the statistical relationship between N_{ij} and $N(m)$, and it is the only factor that is dependent on i and j . Now we consider four examples of N_{ij} : N_{11} , N_{01} , N_{10} and N_{00} . Their expressions can be derived by calculating the specific $S_{ij}(m)$ values as follows:

(1) $N_{00}(m)$. If there is no proton observed on both A-side and C-side AFP detectors, all the interactions should be of the configuration of P_0 , so the expression of S_{00} is given by:

$$S_{00} = P_0^m. \quad (4.4)$$

(2) $N_{10}(m)$. Here, only one proton on the A-side is observed, indicating that the only interaction type of configuration P_A can contribute protons, and all the other interactions are of the configuration of P_0 , so the expression is

$$S_{10} = mP_AP_0^{m-1}. \quad (4.5)$$

(3) $N_{01}(m)$. Analogous to the above, only one proton on the C-side is observed, indicating the only contributing interaction is of type P_C , and all the other interactions are of type P_0 , resulting in the expression:

$$S_{01} = mP_CP_0^{m-1}. \quad (4.6)$$

(4) $N_{11}(m)$. For this configuration, there are two possible classes of contributions. The first is where the P_{AC} interaction type provides the two observed protons, with all the other interactions are of the P_0 type, or alternatively, where the two protons come independently from one P_A interaction and one P_C interaction, and all others are of the P_0 type. These two contributions resulting in the following expression for S_{11} :

$$S_{11} = mP_{AC}P_0^{m-1} + m(m-1)P_AP_CP_0^{m-2}. \quad (4.7)$$

Accounting for the possible ways in which a single proton-proton collision could result in the four possible configurations of proton signature observed in AFP detector, and the relationship to the total interaction rate and number of simultaneous proton-proton collisions presented in equation 4.2 and equation 4.3, we can now derive the following relationships between the measured quantities and the underlying physical parameters of interest:

$$N_{00}(m) = N_0 \frac{\mu^m}{m!} e^{-\mu} P_0^m, \quad (4.8)$$

$$N_{10}(m) = N_0 \frac{\mu^m}{m!} e^{-\mu} m P_A P_0^{m-1}, \quad (4.9)$$

$$N_{01}(m) = N_0 \frac{\mu^m}{m!} e^{-\mu} m P_C P_0^{m-1}, \quad (4.10)$$

$$\begin{aligned} N_{11}(m) &= N_0 \frac{\mu^m}{m!} e^{-\mu} m(m-1) P_A P_C P_0^{m-2} \\ &+ N_0 \frac{\mu^m}{m!} e^{-\mu} m P_{AC} P_0^{m-1}. \end{aligned} \quad (4.11)$$

4.3 Cancellation of Actual Number of Proton-proton Interactions Per Bunch Crossing

The equations derived above describe the relationship between the underlying probabilities of proton-proton interactions and the number of simultaneous proton signature. However, the actual number of proton-proton interactions per bunch crossing, m , follows a distribution which has a mean value of μ . Therefore, to simplify the equations, the expressions can be recast to remove dependence on the quantity, m .

In order to do this, we notice that in considering all possible m values from zero to infinity and using Tolor's theorem, expressions for the sum of all observed yields, N_{ij} , can be derived as follows:

$$N_{00} = \sum_m N_{00}(m) = N_0 e^{-\mu} \sum_m \left(\frac{\mu^m}{m!} P_0^m \right) = N_0 e^{\mu(P_0-1)}, \quad (4.12)$$

$$N_{10} = \sum_m N_{10}(m) = N_0 e^{-\mu} P_A \sum_m \left(\frac{\mu^m}{m!} m P_0^{m-1} \right) = N_0 \mu P_A e^{\mu(P_0-1)}, \quad (4.13)$$

$$N_{01} = \sum_m N_{01}(m) = N_0 e^{-\mu} P_C \sum_m \left(\frac{\mu^m}{m!} m P_0^{m-1} \right) = N_0 \mu P_C e^{\mu(P_0-1)}, \quad (4.14)$$

$$\begin{aligned} N_{11} = \sum_m N_{11}(m) &= N_0 e^{-\mu} \sum_m \left[\frac{\mu^m}{m!} m(m-1) P_A P_C P_0^{m-2} + \frac{\mu^m}{m!} m P_{AC} P_0^{m-1} \right] \\ &= N_0 \mu (P_{AC} + \mu P_A P_C) e^{\mu(P_0-1)}. \end{aligned} \quad (4.15)$$

From these simplified equations and noticing common factors, we can ultimately derive the following relationship between the underlying event probabilities and various event counts, and the average number of interactions per bunch crossing.

$$P_A = \frac{N_{10}}{\mu N_{00}}, \quad (4.16)$$

$$P_C = \frac{N_{01}}{\mu N_{00}}, \quad (4.17)$$

$$P_{AC} = \frac{N_{11}}{\mu N_{00}} - \mu P_A P_C, \quad (4.18)$$

$$P_0 = 1 - P_A - P_C - P_{AC}. \quad (4.19)$$

In a subsequent data analysis we will determine the N_{ij} values, from which the P_A , P_C , P_{AC} , and P_0 can be experimentally determined with a purely data-driven technique using the equations above.

4.4 Deductions from the Probabilistic Model

Among all of the four number of simultaneous proton signatures given above, N_{11} is the most essential one. Because only the configuration of N_{11} contains the interaction of interest, which is the proton-proton diffractive interaction with both protons remain

intact. All the others, including the configurations of N_{01} , N_{10} , and N_{00} , only contribute to the pile-up background events, for they only contain single diffraction processes. [19]

As is shown in equation 4.15, there are two terms in the expression of N_{11} , representing the contributions from two classes of configurations. Combined with the theories about proton-proton interactions in LHC introduced in the first chapter, it can be concluded that the term involving P_{AC} stands for the contribution from signal events, while the term involving P_A and P_C stands for the contribution from pile-up background events.

In the data analysis, however, the number of bunch crossings that contain the interaction of interest can not be distinguished from other N_{11} events. Therefore, the most important deduction from the probabilistic model is the ratio of pile-up events in all of the N_{11} bunch crossings. The ratio is defined as

$$R_{pile-up} = \frac{N_{11}^{pile-up}}{N_{11}} = \frac{N_0 \mu (\mu P_A P_C) e^{\mu(P_0-1)}}{N_0 \mu (P_{AC} + \mu P_A P_C) e^{\mu(P_0-1)}} = \frac{\mu P_A P_C}{P_{AC} + \mu P_A P_C}, \quad (4.20)$$

where the $N_{11}^{pile-up}$ is the contribution from pile-up events in the number of simultaneous proton signature N_{11} .

4.5 Emulation of the Probabilistic Model

A C++ based simulator is written to test the conclusion of the probabilistic arithmetic shown in equations starting from 4.16. The program takes various input underlying probabilities, P_A , P_C , P_{AC} and P_0 , as well as total event number N_0 , to simulate the observed number of simultaneous proton signature, N_{00} , N_{10} , N_{01} and N_{11} , from which the simulated underlying probabilities can be calculated by applying the formalism established above. Then it fits a constant to the simulated underlying probabilities with respect to different values of average number of interactions per bunch crossing (μ), from which, by comparing the difference between the input probabilities and simulated probabilities with the uncertainties, the effectiveness of the formalism can be confirmed.

Another simulation operating on the program exploits a fixed input efficiency value for both A-side and C-side detectors, as well as all the input parameters used in the first simulation, to test the effect of detection efficiency. The techniques applied

here are similar to the first simulation, with the only difference that the detection efficiency is considered for each proton generated. Finally, a linear fitting is applied to the simulated underlying probabilities with respect to different values of average number of interactions per bunch crossing (μ), from which the effect of detection efficiency can be tested by comparing the slope values of fitted lines with 0.

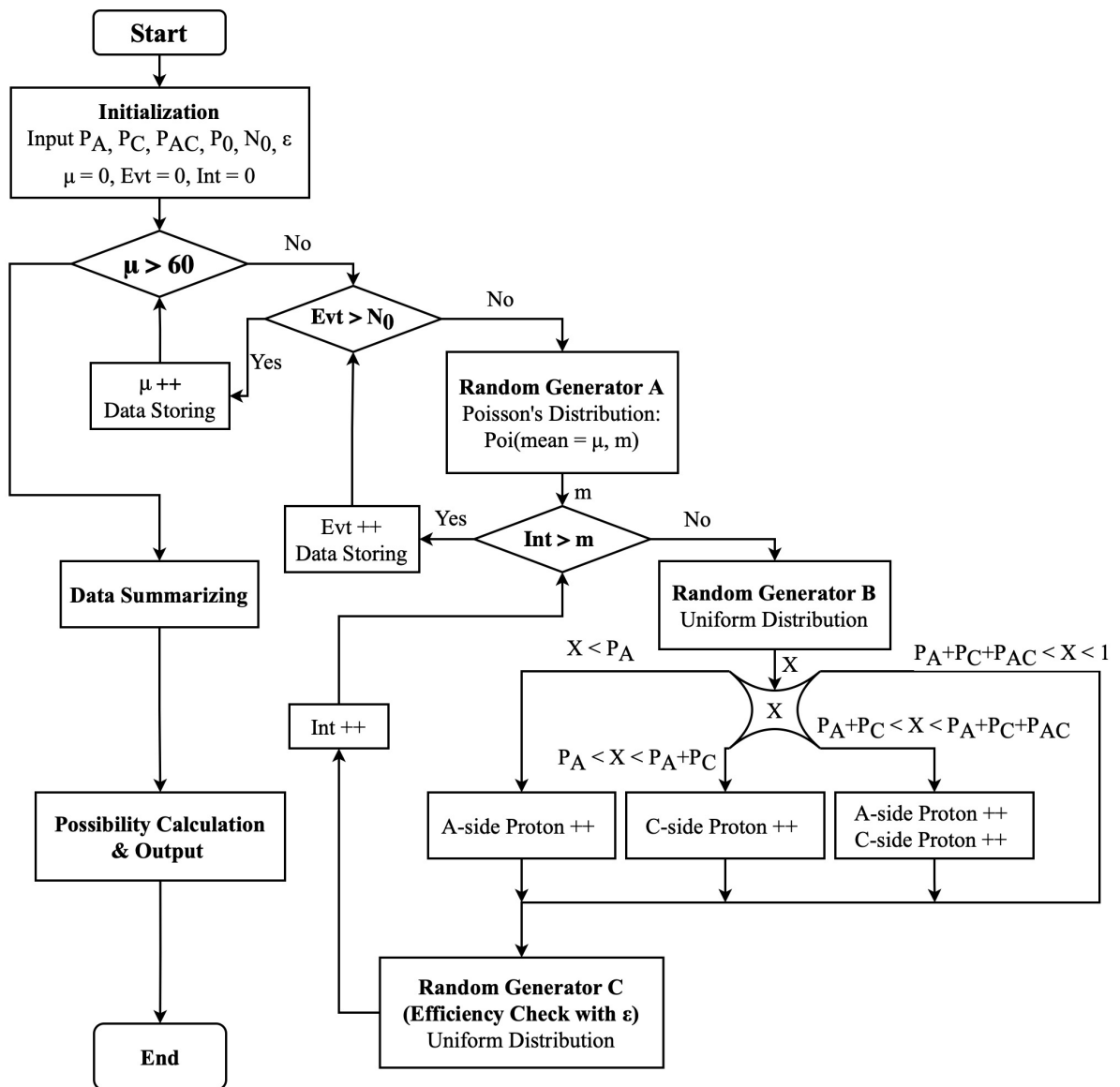


Figure 4.1: Flow chart of the simulator program. The simulator structure is made up of 3 parts: the initialization part, the 3-layer loops, and the finalization part.

The structure of the program, as is described in Figure 4.1, is made up of three loops, shown as below:

In the initialization part, input values of P_A , P_C , P_{AC} , P_0 , total bunch crossing N_0 , and fixed detecting efficiency ε are needed. Then the program will iterate on μ , N_0 , and number of proton-proton interactions in each bunch crossing. In the loop, a random number between 0 and 1 is generated from a uniform random generator to determine the configuration of each proton-proton interaction in each bunch crossing. Before the end of loop, with another random number between 0 and 1, the detecting efficiency can be considered by comparing the random number with ε . If the random number is larger than ε , it means a proton is neglected by the detector and the proton numbers in this bunch crossing will be reduced.

Finally, at the end of the emulation program, we can get the observed N_{00} , N_{01} , N_{10} , and N_{11} values, which can be used to derive the output values of P_A , P_C , P_{AC} , and P_0 by applying the equations starting from 4.16 in the finalization part.

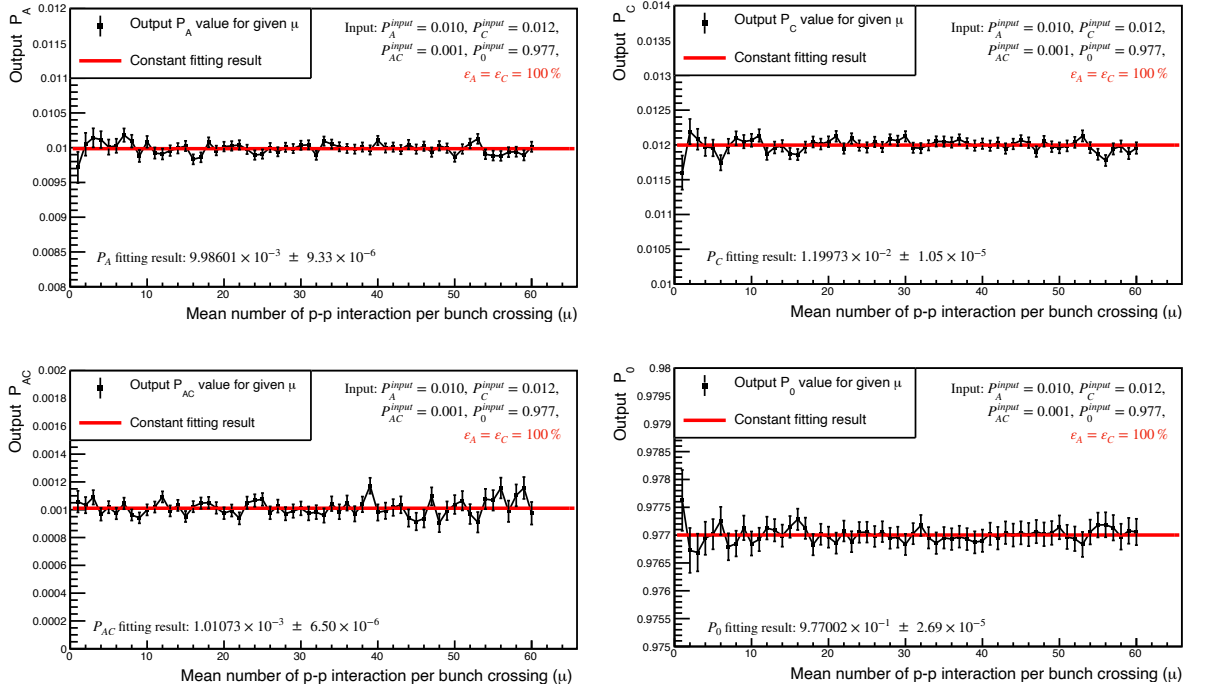


Figure 4.2: Comparisons between output probabilities from the simulator (markers) and the constant fitting, and the input parameter values, as well as the final constant fitting results are shown.

In order to validate the probabilistic model, we firstly set the input probabilities as $P_A = 0.010$, $P_C = 0.012$, $P_{AC} = 0.001$, $P_0 = 0.977$, and number of simultaneous proton signature as $N_0 = 200000$, and detecting efficiency as $\varepsilon = 1.00$. With such settings one can expect the output probabilities to be constant and close to the input values. The

comparisons between input probabilities and output probabilities from the simulator are shown in Figure 4.2, from which we can conclude that for all of the four underlying probabilities, the output values of the simulator (markers) are not deviating from the corresponding input values much, and the differences between constant fitting results (red lines) and input probability values are small, compared with the propagated uncertainties shown as the error bars. That is to say, the probabilistic model is proved to be valid.

We then consider an input detecting efficiency $\varepsilon = 0.9$ with other input parameters unchanged. The plots of output probabilities vs. μ , together with the linear fitting curves are shown in Figure 4.3. The slope values consistent with 0 indicate the validity of the assumption that all of the predefined probabilities are constant with respect to the average number of proton-proton interactions per bunch crossing, μ , and with a detecting efficiency not equal to 1, the probabilities should still be constant with respect to μ .

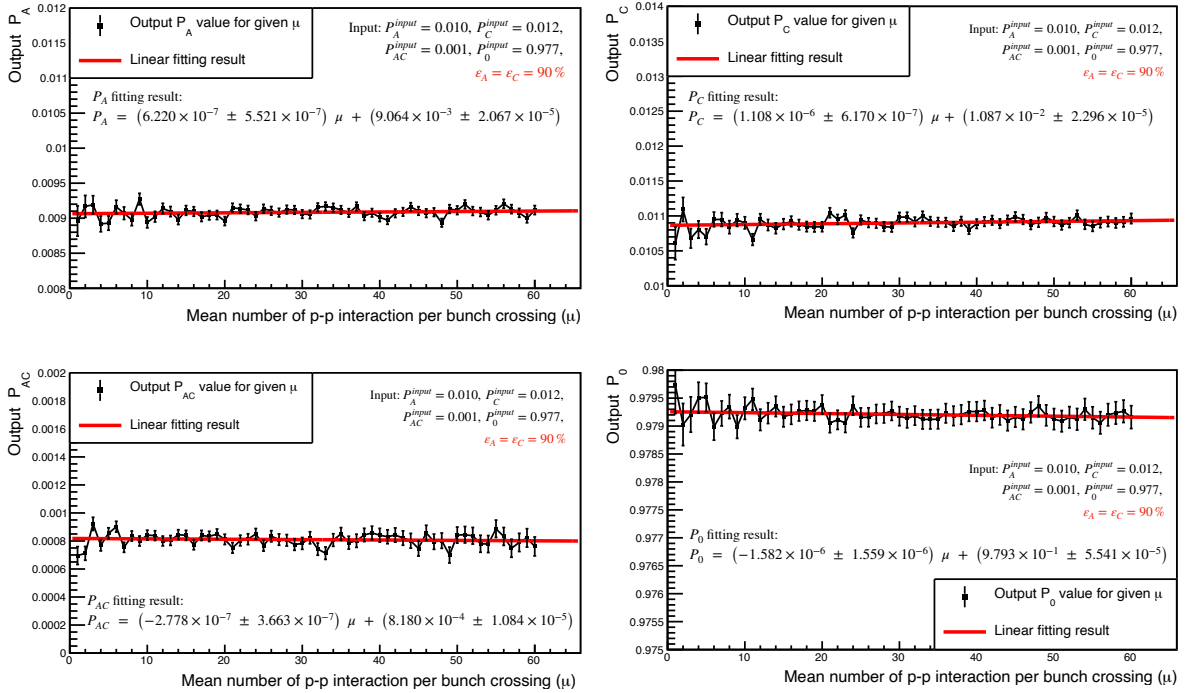


Figure 4.3: Plots of output probabilities as functions of μ values when detecting efficiencies $\varepsilon \neq 1$ are involved, together with their linear fitting curves. The markers represent the output probability values, and the red curves are linear fitting results of the output probabilities.

As for other parameters, as is shown in figure 4.4, comparisons between input underlying probability values and output probabilities are given. According to the linear fitting results which have slopes close to 1, the differences between output probabilities and input probabilities are small (uncertainties propagated are too small to be shown on the plots), and it can be concluded that the simulator is eligible to model the proton-proton interactions and their probabilities, and the correctness of the probability arithmetic is proved.

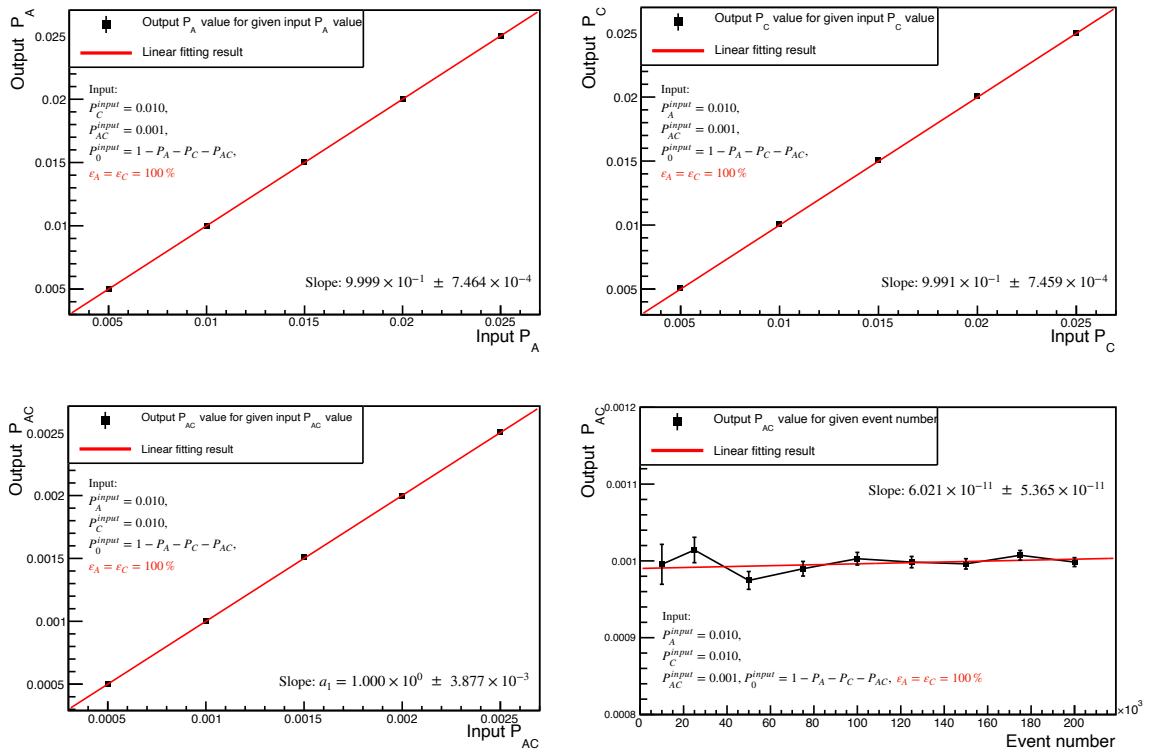


Figure 4.4: Comparison between the input probabilities and corresponding output probabilities, together with the comparison between the output P_{AC} and input event number.

Figure 4.4 shows the output probability P_{AC} as a function of the simulated event number N_0 . As N_0 increases, the uncertainty of output P_{AC} decreases, oscillating around the input P_{AC} value slightly, which shows the consistency of output probabilities when using different amount of event numbers.

Figure 4.5 shows different output probabilities (P_A , P_C and P_{AC} , for there are only three independent probabilities) with different input detection efficiencies, ε . Here the efficiencies of A-side and C-side detectors are considered the same, which means $\varepsilon = \varepsilon_A = \varepsilon_C$, and ε varies from 50% to 100%. With linear fitting applied to output P_A and P_C , and second order polynomial fitting applied to P_{AC} , the good fitting results indicate that the output P_A and P_C could be proportional to the efficiencies and the output P_{AC} could be proportional to ε^2 , i.e.

$$P_A^{out} = P_A^{in} \varepsilon, \quad (4.21)$$

$$P_C^{out} = P_C^{in} \varepsilon, \quad (4.22)$$

$$P_{AC}^{out} = P_{AC}^{in} \varepsilon^2, \quad (4.23)$$

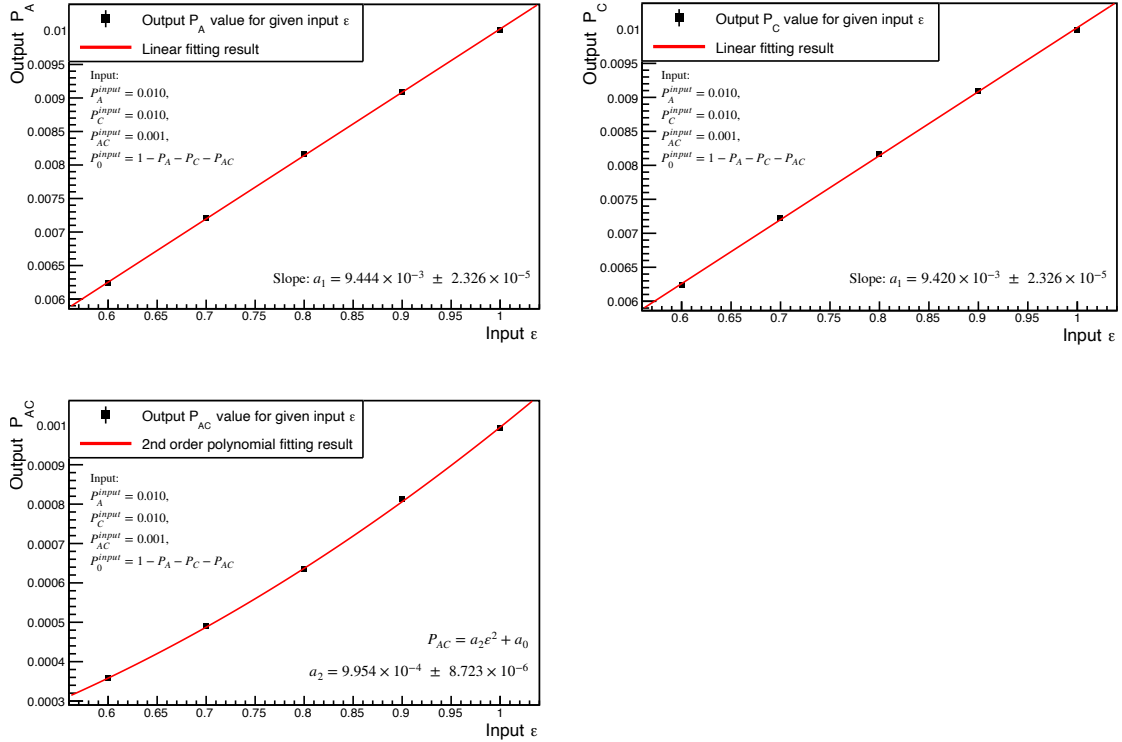


Figure 4.5: Plots of output probabilities as functions of ε values when other probabilities are constant. For different probabilities, fitting models involved are different.

Chapter 5

Data Analysis

In this chapter, the process and results of the AFP data analysis will be discussed. Firstly, a description of the data used in the analysis is given. It includes the introduction to the triggers and selection criteria applied in the data, which consists of the introduction to the ATLAS trigger menu and the AFP Good Run List (GRL). Then in the second section, the analysis of AFP data is demonstrated. In this section, distributions of several kinematics quantities are presented, and the probabilistic model presented in the previous chapter is used to describe the data collected by the AFP and the underlying probabilities of the model are calculated. The probabilities are found to be dependent on the number of pile-up interaction and further analysis is carried out to investigate the causes.

5.1 Event Selection

As introduced in chapter 3, an integrated luminosity of 46.4 fb^{-1} was recorded by ATLAS in 2017, 32.0 fb^{-1} of which was recorded with AFP [38]. However, not all of the 32.0 fb^{-1} is useful data. Instead, only 19.2 fb^{-1} are eligible for the analysis, and a subset of which is used in this research. Two separate selections are applied to the data set: trigger menu and Good Run List (GRL), separately introduced in following sections.

5.1.1 ATLAS Trigger Menu

The trigger menu of ATLAS in 2017 is based on several building blocks [41]:

Primary trigger menu: List of triggers that are used for physics measurements. It is the core trigger menu, and typically unprescaled of different runs.

Support trigger menu: List of triggers that are used for efficiency measurements, detector performance analysis, and background monitoring.

Alternative trigger menu: Algorithms of alternative online reconstruction, which is complementary to the primary and support triggers.

Backup trigger menu: A set of triggers tighter than primary ones, in case the primary triggers are too loose and the trigger rate is too high.

Calibration trigger menu: List of triggers used for detector calibration.

In our analysis, apart from the physics measurement, no extra measurement (efficiency measurements, background measurements, ATLAS performance, etc) is needed, and the primary triggers are applied. Table 5.1 shows the structure of the main triggers in 2017 and some typical trigger selections applied. The complete list of 2017 trigger menu is a long list considering all the physical and technical limitations in L1 triggers and HLT triggers, which can not be listed in details. In all, the total rate of the full trigger menu is 1550 Hz, which includes the triggers not listed in the table.

5.1.2 Good Run List (GRL)

Data is recorded in "runs", corresponding to a specific period of time when ATLAS is recording data. Every run has a non-repeating 6-digit number assigned to it, which is called the "run number". Each run can be further divided in to several parts, and in each part, the instantaneous luminosity can be considered constant. These parts are called "luminosity blocks" (LBs). In general, one LB refers to the data collected in 60 seconds [42].

In some LBs, detector components can be compromised and record sub-standard data. The Good Run List (GRL) is used to get the data that is of sufficient quality for data analysis. The GRL is a set of XML [43] files that contains a list of LBs certified for physics analysis.

The good run list applied in the data set we use has two parts, the ATLAS GRL and AFP GRL. ATLAS GRL is produced by querying the data and reduce the integrated

Trigger	Typical offline selection	Trigger Selection		Level-1 Peak	HLT Peak
		Level-1 (GeV)	HLT (GeV)	Rate (kHz)	Rate (Hz)
				$L = 1.7 \times 10^{34} \text{ cm}^{-2} \text{ s}^{-1}$	
Single leptons	Single isolated μ , $p_T > 27 \text{ GeV}$	20	26 (i)	15	180
	Single isolated tight e , $p_T > 27 \text{ GeV}$	22 (i)	26 (i)	28	180
	Single μ , $p_T > 52 \text{ GeV}$	20	50	15	61
	Single e , $p_T > 61 \text{ GeV}$	22 (i)	60	28	18
	Single τ , $p_T > 170 \text{ GeV}$	100	160	1.2	47
Two leptons	Two μ , each $p_T > 15 \text{ GeV}$	2×10	2×14	1.8	26
	Two μ , $p_T > 23, 9 \text{ GeV}$	20	22, 8	15	42
	Two very loose e , each $p_T > 18 \text{ GeV}$	2×15 (i)	2×17	1.7	12
	One e & one μ , $p_T > 8, 25 \text{ GeV}$	20 (μ)	7, 24	15	5
	One e & one μ , $p_T > 18, 15 \text{ GeV}$	15, 10	17, 14	2.0	4
	One e & one μ , $p_T > 27, 9 \text{ GeV}$	22 (e, i)	26, 8	28	3
	Two τ , $p_T > 40, 30 \text{ GeV}$	20 (i), 12 (i) (+jets, topo)	35, 25	5	61
	One τ & one isolated μ , $p_T > 30, 15 \text{ GeV}$	12 (i), 10 (+jets)	25, 14 (i)	2.1	10
One τ & one isolated e , $p_T > 30, 18 \text{ GeV}$	12 (i), 15 (i) (+jets)	25, 17 (i)	4	15	
Three leptons	Three loose e , $p_T > 25, 13, 13 \text{ GeV}$	$20, 2 \times 10$	$24, 2 \times 12$	1.3	< 0.1
	Three μ , each $p_T > 7 \text{ GeV}$	3×6	3×6	0.2	6
	Three μ , $p_T > 21, 2 \times 5 \text{ GeV}$	20	$20, 2 \times 4$	15	8
	Two μ & one loose e , $p_T > 2 \times 11, 13 \text{ GeV}$	2×10 (μ)	$2 \times 10, 12$	1.8	0.3
	Two loose e & one μ , $p_T > 2 \times 13, 11 \text{ GeV}$	$2 \times 8, 10$	$2 \times 12, 10$	1.7	0.1
One photon	One loose γ , $p_T > 145 \text{ GeV}$	22 (i)	140	28	43
Two photons	Two loose γ , $p_T > 55, 55 \text{ GeV}$	2×20	50, 50	2.6	6
	Two medium γ , $p_T > 40, 30 \text{ GeV}$	2×20	35, 25	2.6	17
	Two tight γ , $p_T > 25, 25 \text{ GeV}$	2×15 (i)	2×20 (i)	1.7	14
Single jet	Jet ($R = 0.4$), $p_T > 435 \text{ GeV}$	100	420	3.3	33
	Jet ($R = 1.0$), $p_T > 480 \text{ GeV}$	100	460	3.3	24
	Jet ($R = 1.0$), $p_T > 450 \text{ GeV}$, $m_{\text{jet}} > 50 \text{ GeV}$	100	$420, m_{\text{jet}} > 40$	3.3	29
E_T^{miss}	$E_T^{\text{miss}} > 200 \text{ GeV}$	50	110	5	110
Multi-jets	Four jets, each $p_T > 125 \text{ GeV}$	3×50	4×115	0.5	16
	Five jets, each $p_T > 95 \text{ GeV}$	4×15	5×85	5	10
	Six jets, each $p_T > 80 \text{ GeV}$	4×15	6×70	5	4
	Six jets, each $p_T > 60 \text{ GeV}$, $ \eta < 2.0$	4×15	$6 \times 55, \eta < 2.4$	5	15
b -jets	One b ($\epsilon = 40\%$), $p_T > 235 \text{ GeV}$	100	225	3.3	15
	Two b ($\epsilon = 60\%$), $p_T > 185, 70 \text{ GeV}$	100	175, 60	3.3	12
	One b ($\epsilon = 40\%$) & three jets, each $p_T > 85 \text{ GeV}$	4×15	4×75	5	15
	Two b ($\epsilon = 70\%$) & one jet, $p_T > 65, 65, 160 \text{ GeV}$	$2 \times 30, 85$	$2 \times 55, 150$	1.2	15
	Two b ($\epsilon = 60\%$) & two jets, each $p_T > 65 \text{ GeV}$	$4 \times 15, \eta < 2.5$	4×55	3.2	13
B -Physics	Two μ , $p_T > 11, 6 \text{ GeV}$	11, 6	11, 6 (di- μ)	2.5	47
	Two μ , $p_T > 6, 6 \text{ GeV}$, $2.5 < m(\mu, \mu) < 4.0 \text{ GeV}$	2×6 (J/ψ , topo)	2×6 (J/ψ)	1.6	48
	Two μ , $p_T > 6, 6 \text{ GeV}$, $4.7 < m(\mu, \mu) < 5.9 \text{ GeV}$	2×6 (B , topo)	2×6 (B)	1.6	5
	Two μ , $p_T > 6, 6 \text{ GeV}$, $7 < m(\mu, \mu) < 12 \text{ GeV}$	2×6 (Y , topo)	2×6 (Y)	1.4	10
Total Rate			85	1550	

Figure 5.1: A list of some typical triggers in the primary physics trigger menu and their trigger rates [41].

luminosity to 26 fb^{-1} (integrated luminosity with AFP inserted). Then the AFP GRL is applied with additional requirements to AFP sub-detector information [38]:

- All AFP stations need to be inserted to their nominal data taking position.
- In each AFP station, high voltage of at least two SiT layers must be turned on.
- No data acquisition problem observed [44].

After all of the requirements above are imposed, the LBs that are good for physics analysis are selected, and the luminosity is reduced to 19.2 fb^{-1} . However, in this analysis, 55 specific runs are selected from the GRL for further analysis, because only these runs are in standard and high pile-up ($18 < \mu < 60$) conditions.

5.1.3 Proton Selection

In our analysis, after the general selection is applied, it is still possible that the AFP data in some runs is not usable, because some proton tracks recorded by the AFP come from noises. So we still need a set of selection for the AFP data to make sure the proton tracks in AFP are reconstructed with good quality [38].

The proton track selection criteria is as follows:

- For the track reconstruction, the maximum distance between the clusters from different SiT layers on xy plane in which they are considered coming from the same track is 0.5 mm.
- Protons are required to satisfy "medium" quality criteria. There are three types of quality criteria in total: "loose", "medium" and "tight". "Loose" type means there is no limitation for the number of SiT layers that have hit clusters; "Medium" means that the number of SiT layers that have at least one hit cluster must be no-fewer-than the minimum value, which is 2; "Tight" type means, apart from the limitation commanded by the "medium" type, the number of SiT layers that have multiple hit clusters must be zero.
- Tracks need to be reconstructed in both the NEAR and FAR stations. For each proton track reconstructed, the minimum distance between the track reconstructed from NEAR station and that from FAR station on xy plane must be less than 2.0 mm, otherwise the two tracks can not be considered coming from one proton.

After the limitation to the reconstruction imposed as above, the reconstructed proton tracks remain in the data set are all considered as "good" proton tracks. After all the selection, the total number of the events involved in the research is 1.22×10^9 .

In some parts of the following analysis, it is required that there is only one proton track on the A-side and only one on the C-side. Additional statements will be given when this extra limitation is applied.

5.2 Results of Data Analysis

The data analysis is divided into two parts. In the first part, distributions of several kinematics quantities is presented for events with exactly one proton on each side of AFP. This shows the basic performance of AFP. In the second section, the probabilistic model established in previous chapters is used to describe the data, and the underlying probabilities of forward proton production in the model are calculated.

5.2.1 Distributions of Physical Quantities and Performance of the AFP

In this section, quantities including the fractional momentum loss, average number of proton-proton interactions per bunch crossing, missing mass distribution and number of A-side and C-side protons are shown.

Average Proton-proton Interactions Number Per Bunch Crossing

The distribution of average proton-proton interactions number per bunch crossing, μ is shown in figure 5.2. In experiment, the actual number of proton-proton interactions for each event, m , can be measured by the inner detector using the number of vertices. For each luminosity block, the average number of proton-proton interactions per bunch crossing, μ , is directly derived from the instantaneous luminosity using equation 3.3 experimentally. Since the actual number of proton-proton interactions for each event, m , is already eliminated mathematically, we only need the μ distribution. The distribution shows that, in the 55 runs we use, all the events have μ values in the range of $18 < \mu < 60$.

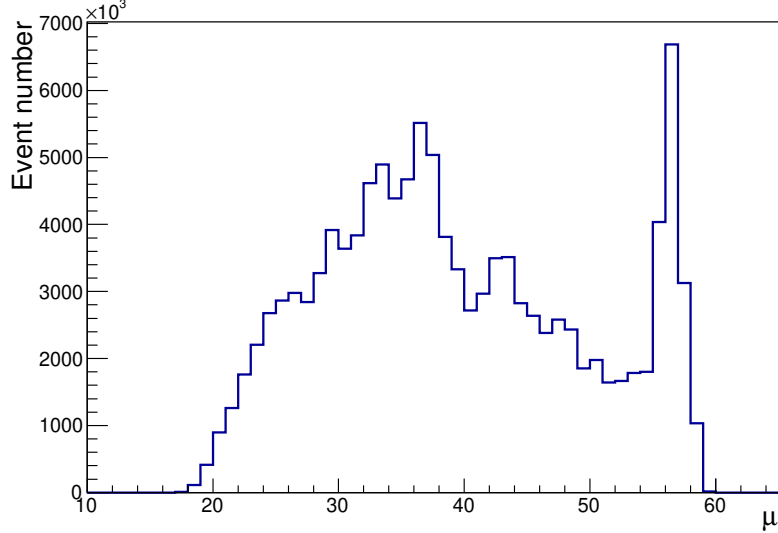


Figure 5.2: The distribution of average proton-proton interactions number per bunch crossing found in the data analysis, which is consistent with the published result of ATLAS in 2017 [32].

The events can be divided into two groups: events with a continuum pile-up shown as the distribution in $10 < \mu < 50$, and events with higher pile-up which is shown as the peak near $\mu = 60$. This shape is a result of "luminosity leveling", which refers to the techniques used to control the luminosity. As an example, the offset between the two crossing proton beams can be used to level the luminosity on LHC [45].

In August 2017, a problem was identified in sector 16L2 of LHC. The treatment of this problem set off a series of further problems. As a result, LHC finally reached a record luminosity of $L = 2.08 \times 10^{34} \text{ cm}^2\text{s}^{-1}$ and the pile-up also reached a unprecedented level of $\mu = 80$, which produced an excessive strain to the computation resources. In order to fix this, ATLAS requested a luminosity leveling at $L = 1.56 \times 10^{34} \text{ cm}^2\text{s}^{-1}$, and μ remained at about 60 in this period of time, which produced the peak at $\mu = 60$ presented on figure 5.2.

In 2017, there are three types of runs with different pile-up conditions: low pile-up events with μ close to 0, standard pile-up events with continuum μ in $10 < \mu < 50$, and high pile-up events with μ concentrated near $\mu = 60$. According to the distribution, the 55 runs we use only contain continuum pile-up and high pile-up events.

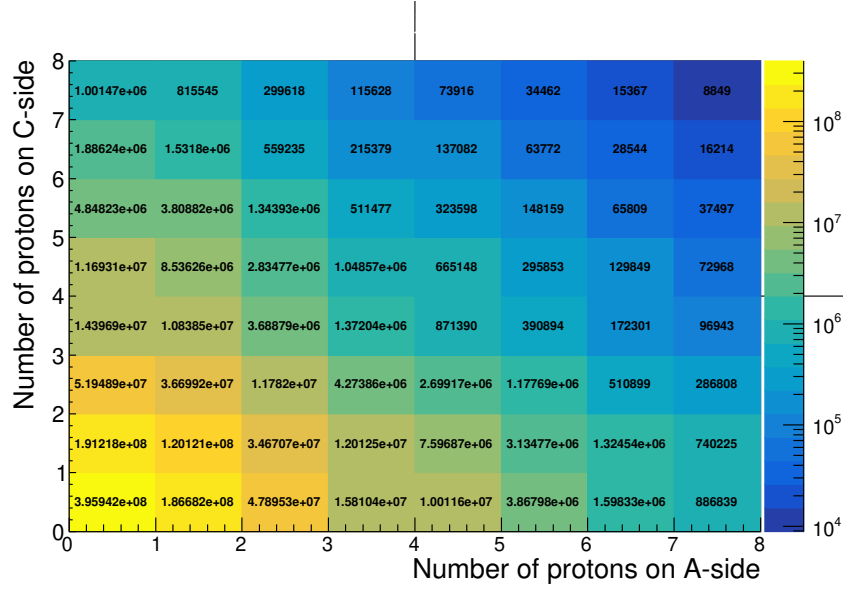


Figure 5.3: The number of protons reconstructed on each side of AFP, given by data analysis. Number of events in each channel is represented by colour, which is given in logarithm scale.

Number of Events with Different Number of A-side Protons and C-side Protons

The number of events with different number of protons on each side of AFP are shown in figure 5.3. It shows that most events has a proton number no larger than 2 on both sides, and the events with no protons on each side have the largest fraction.

Although the events with fewer than two protons on each side take the majority, some ab"normal" events with proton number on each side be higher than three still exist. For example there are 8849 events recorded to have seven forward protons detected on each side of AFP, which is unexpected and the only possible origin of these events is the pile-up background.

Fractional Momentum Loss for Protons

With the four-momentum of protons measured by AFP, the momentum loss of protons on A-side and C-side, ξ_A and ξ_C can be calculated using equation 2.1. In figure 5.4, the distributions of ξ_A and ξ_C are presented for those events with exactly one proton detected on each side of AFP. In the results, a plateau shape shows up for both ξ_A and ξ_C , the maximum ranges of ξ_A and ξ_C distributions are measured to be $0.025 < \xi_A < 0.12$ and $0.025 < \xi_C < 0.12$, but because of their relatively flat

distribution shown in $0.10 < \xi_A < 0.12$ and $0.10 < \xi_C < 0.12$, an effective range of ξ selected for both A-side and C-side protons on AFP should be: $0.025 < \xi_{A/C} < 0.10$, which is consistent with the conclusion given in previous researches like the results in the AFP Technical Design Report [19] shown in figure 3.8.

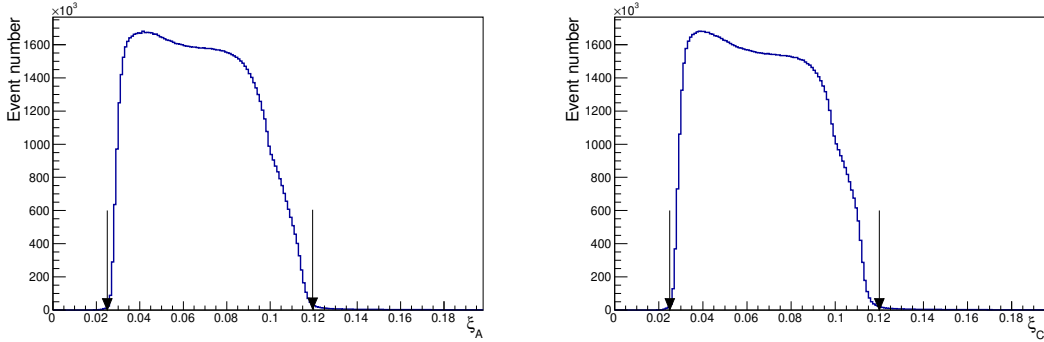


Figure 5.4: The distributions of ξ_A (left) and ξ_C (right) for events with only one proton detected on both A-side and C-side given by data analysis, with the maximum ranges of ξ_A and ξ_C to be $0.025 < \xi_A < 0.12$ and $0.025 < \xi_C < 0.12$. Here the black arrows denote the the position of 0.025 and 0.12.

The two curves both have a rapid turn on at $\xi_{A/C} = 0.025$ and a gentle turn off in the region $0.10 < \xi_C < 0.12$. This shape comes from the acceptance of the AFP detector. According to the AFP technical design report, the x coordinates of the projection of forward proton tracks on the SiT planes are positively correlated to the fractional momentum loss ξ , and the AFP SiT layers only cover a limited area on xy-plane. Therefore, the proton tracks with $\xi < 0.02$ and proton tracks with $\xi > 0.12$ can not be accepted by AFP. Additionally, the acceptance of AFP is run dependent, which could account for the gentle turn off in the region $0.10 < \xi_{A/C} < 0.12$.

Missing Mass Distribution

Figure 5.5 shows the missing mass distribution of the events with one proton detected on each side of AFP. The curve shows a continuous distribution in the range of $350 \text{ GeV} < M_{miss} < 1.5 \text{ TeV}$, which is consistent with the prediction given by ξ_A and ξ_C measurement given in 5.2.1 and the relationship between fractional momentum loss and missing mass presented in equation 2.7.

From the smooth continuum shown on the histogram, no pattern (e.g. resonance structures) is observed on the missing mass spectrum. As is discussed in chapter

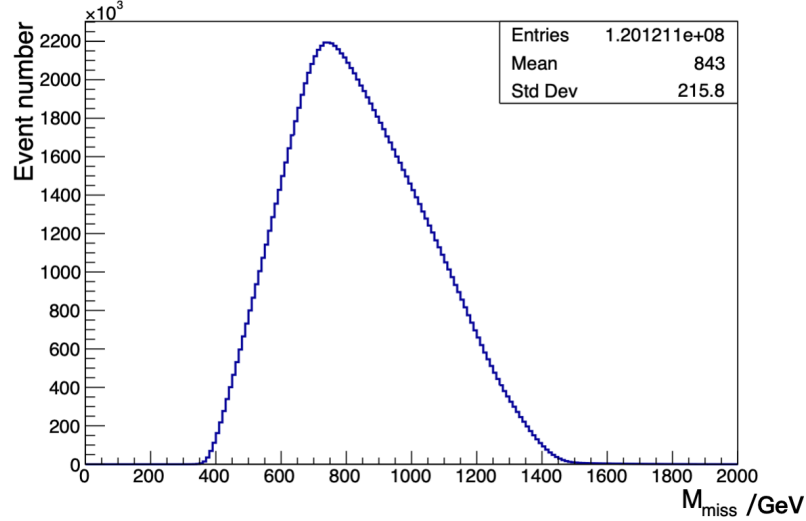


Figure 5.5: Histogram presenting the missing mass distribution of events with only one proton detected on both A-side and C-side, given by data analysis.

2, in proton-proton interactions in the ATLAS, ideally only elastic scattering and DPE processes have contribution to the events presented in figure 5.5. However, two protons in opposite directions separately from two SD processes can also be misjudged as the signal, which is called the pile-up background.

5.2.2 Event Mixing

In order to determine the missing mass distribution of pile-up background events, an "event mixing" method is applied. By applying this method, all the events with only one proton detected on each side of AFP (these events are called "normal" events) can be transformed into manually "mixed" pile-up background events. Then these "mixed" events can simulate the pile-up background events.

The procedure of the event mixing technique is as follows. Firstly, all the "normal" events are numbered from 1 to N_{11} , where N_{11} is the total number of events with one proton on each side. Then as is presented in 5.6, the A-side proton track of the i -th normal event, $\text{Track}_A(i)$, is combined with the C-side proton track of the $(i + 1)$ -th normal event, $\text{Track}_C(i + 1)$, forming the i -th "mixed" event (index i is circulated from 1 to $N_{11} - 1$). Finally, $N_{11} - 1$ "mixed" events are produced. In each "mixed" event, the A-side proton and the C-side proton separately come from two different "normal" events, ensuring all the "mixed" events are, by definition, pile-up background events.

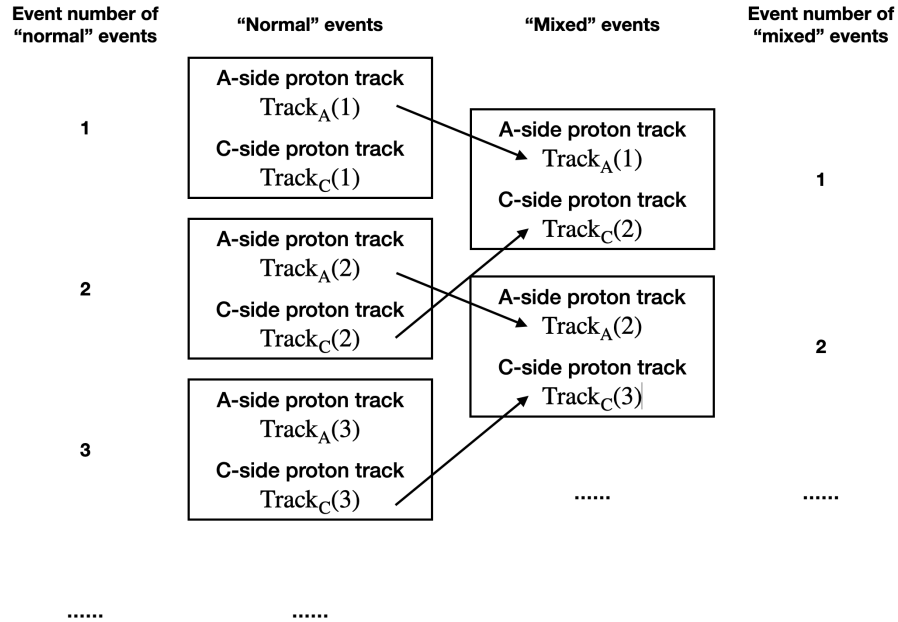


Figure 5.6: The schematic plot of event mixing procedure. Proton tracks in the "normal" events are re-allocated, forming a new batch of "mixed" events.

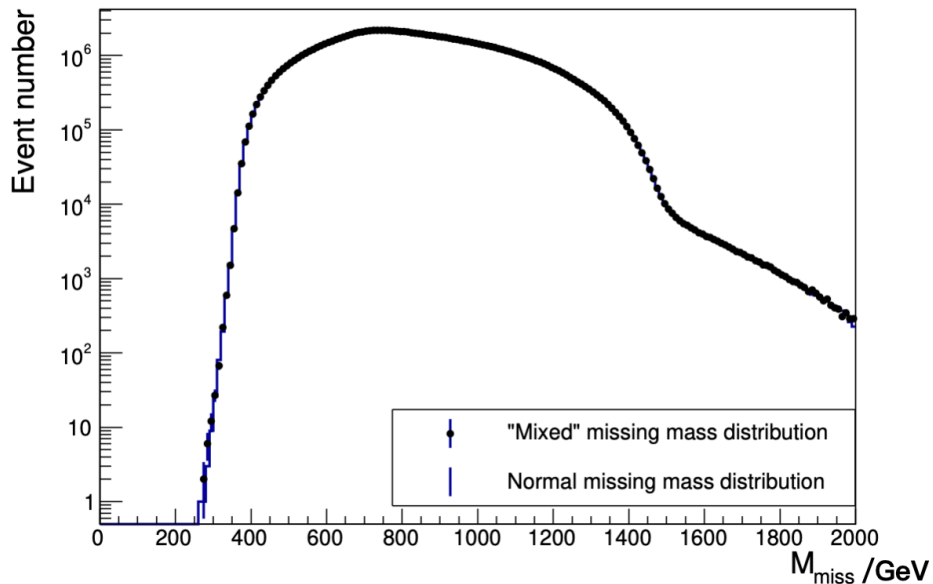


Figure 5.7: The distribution of missing mass as well as the distribution of manually produced "mixed" missing mass, which is drawn in logarithm scale. The normalised missing mass distribution from "mixed" events is presented as the markers, and the rigid line histogram represents the missing mass distribution from "normal" events.

Then the missing mass distributions are separately produced using "normal" events and "mixed" events. Since there are N_{11} "normal" events and $(N_{11} - 1)$ "mixed" events, the distribution of "mixed" events is normalised to the observed yield of "normal" events, N_{11} (the uncertainties are too small to be seen on the figure).

The comparison between the missing mass spectra from "normal" events and "mixed" events is presented in figure 5.7.

The comparison presented in figure 5.7 shows that the line shape of normal missing mass distribution has no observable difference with the pile-up backgrounds, which indicates that the "normal" events are mainly made of pile-up background events.

5.2.3 Application of the Probabilistic Model in Data

In order to calculate the underlying probabilities for the data, the specific N_{ij} values with fixed μ values are needed. Then for each fixed μ , its corresponding probabilities can be derived using equations 4.16 to 4.19, and we can get a relationship between the underlying probabilities (P_A , P_C , P_{AC} , and P_0) and the average proton-proton interaction number per bunch crossing, μ .

In figure 5.8, the probabilities vs. μ values are presented. The errors are presented by an error bar on each point, but they are too small to be seen on the plots. In the region of $\mu < 20$ and $\mu > 55$, anomalous patterns show up because of the numbers of events in these regions are relatively smaller than the events of $20 < \mu < 55$. From the figures we can conclude that all of the underlying probabilities have obvious increasing or decreasing tendencies with respect to μ . A linear fitting line of the form $y = mx + c$ is shown on each histogram. For P_A and P_C , decreasing gradients of $m = -5.5 \times 10^{-5} \pm 1.3 \times 10^{-7}$ are observed, and for P_{AC} , a positive gradient of $m = 7.0 \times 10^{-5} \pm 8.4 \times 10^{-8}$ is observed. This is not expected because the probabilities are defined per proton-proton interaction and there should be no μ dependence, as shown by the simulations presented in chapter 4.

There are several possible causes for the dependency on μ :

The first possible cause is the μ values in events are systematically biased. To examine if this could cause the tendency of probabilities, we compare the original probabilities from the data set with the "shifted" probabilities in which the μ value involved in the calculation is replaced by a slightly shifted μ .

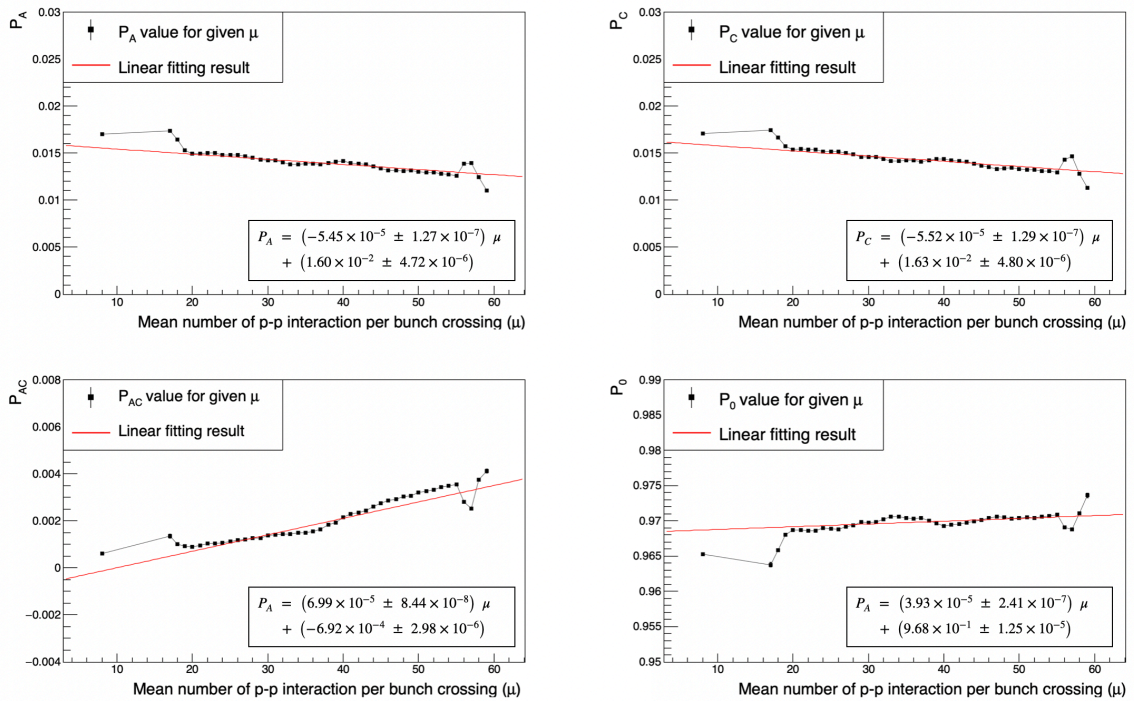


Figure 5.8: Calculated four underlying probabilities as functions of average proton-proton interaction number per bunch crossing. A linear fitting is also applied for each of them, showing non-zero gradients for the probabilities.

Two systematic biases in μ are investigated. (i) an absolute shift in μ : $\mu \rightarrow \mu \pm \Delta\mu$ and (ii) a relative shift in μ : $\mu \rightarrow \mu \cdot (1 \pm \Delta r)$, where $\Delta\mu$ and Δr are constant values.

Figures 5.9 and 5.10 present the relative difference, $\Delta P_X/P_X$ as a function of μ , where ΔP_X is the difference between original probabilities and shifted probabilities caused by a bias in μ . Figure 5.9 shows that with a small absolute shift in μ , probabilities from low- μ region will have larger differences with the original probabilities compared with those from high- μ region. Larger shift in μ present larger values of $\Delta P_X/P_X$. Figure 5.10 shows that with a relative shift applied to μ , a constant relative shift in the probabilities P_A , P_C , and P_{AC} is obtained.

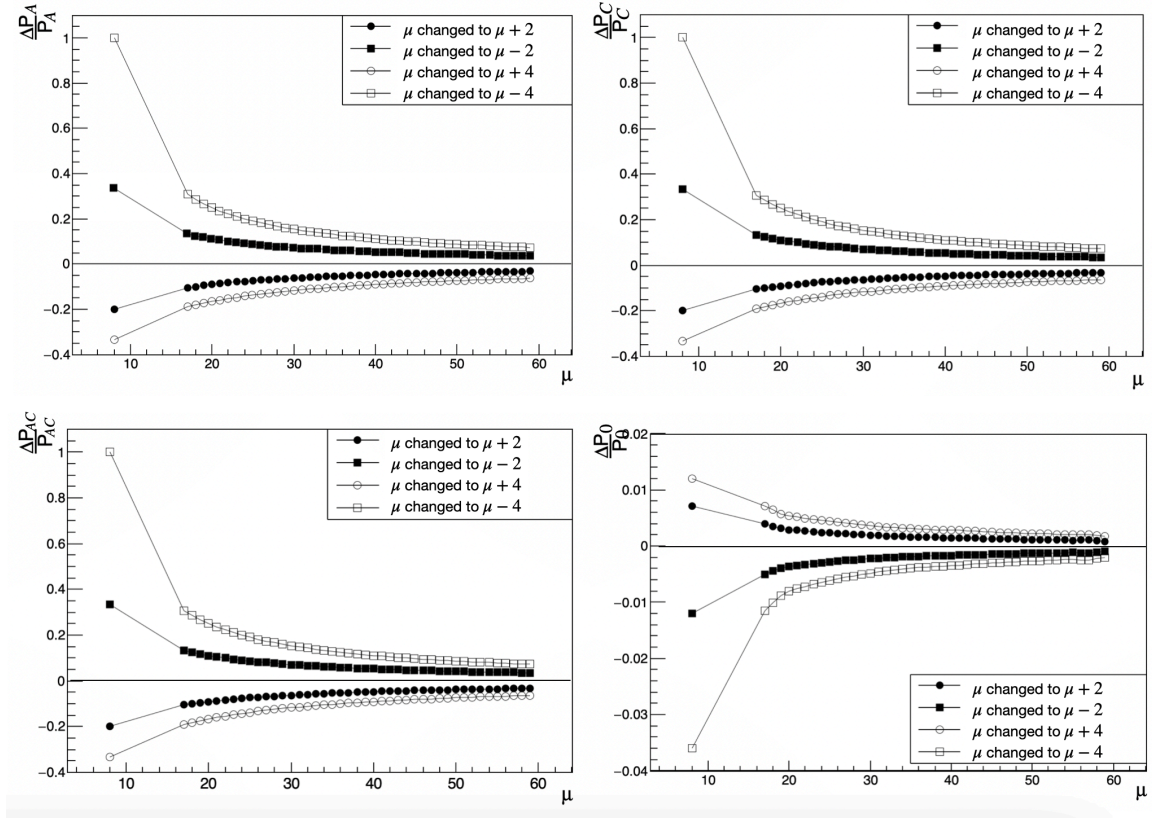


Figure 5.9: Relative differences of underlying probabilities after μ is shifted by an absolute value. Two optional values for the shifting are considered.

Although a constant shift in μ can cause a linear trend in the measured probabilities, the gradient of the probabilities are expected to be all positive or all negative. In the data presented in figure 5.8, the values of P_A and P_C are decreasing with μ , while the P_{AC} has an increasing tendency with μ . Therefore, we conclude that the trend seen in data can not be coming from the biases in μ .

The second possible reason is the existence of detector efficiency. As is tested using simulation in chapter 4, the detection efficiency will be reduced if the detector has an efficiency smaller than 1, which could account for the tendency shows on the figure 5.8.

However, this hypothesis has a lot of defects. Firstly, as is shown in the simulation results in figure 4.3, 4.4, and 4.5, if a constant global efficiency is involved in the calculating process, constant relative differences between the original probabilities and changed ones are expected, and it can not account for the gradient we observed in figure 5.8.

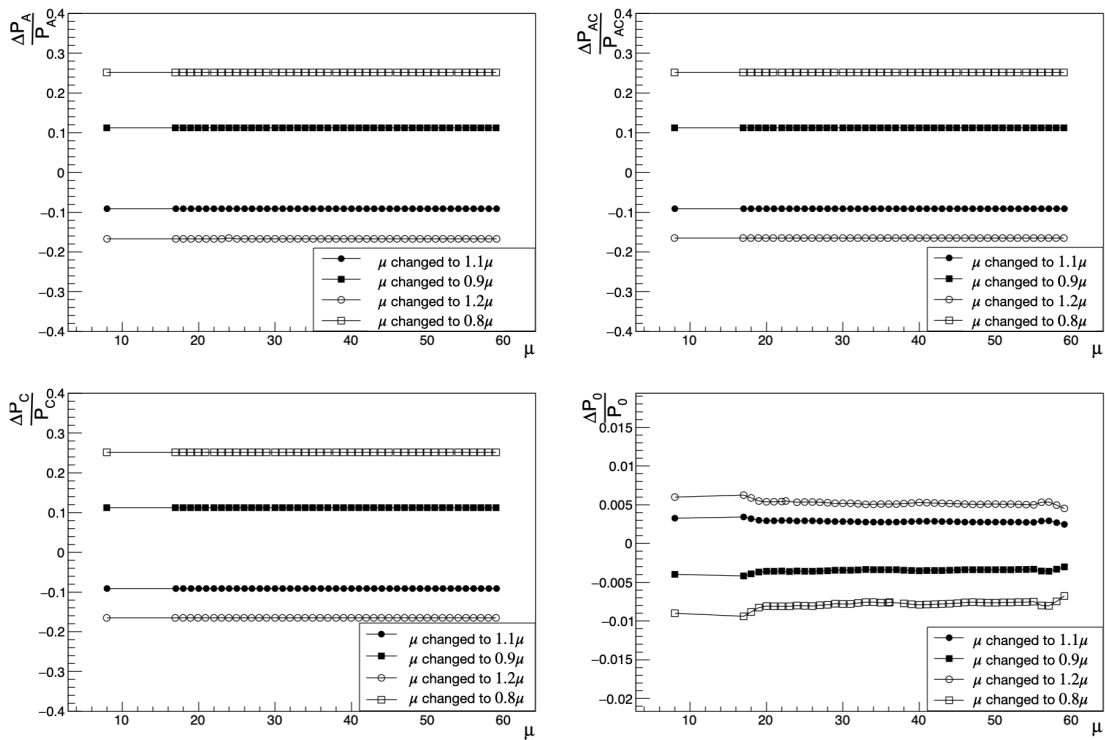


Figure 5.10: Relative differences of underlying probabilities after μ is shifted slightly by a small fraction. Two optional relative values for the shifting are considered.

Secondly, if we introduce a changing efficiency $\varepsilon(\mu)$ that could change with respect to μ , according to the previous simulation, we still expect the gradient values of P_A , P_C , and P_{AC} to be all positive or all negative, which is still in conflict with the observed results in data. Thus, the efficiency can not be a good reason.

The last potential reason for the tendency is the inconsistency of data in different runs. In order to test the differences between probabilities calculated from different

runs, several runs in 2017 are selected and going through the probabilities calculation process separately. Their results of P_A are shown in figure 5.11. The top figure shows the probability P_A vs. μ for different runs, and the bottom figure shows the time position of different runs using arrows in corresponding colours. The arrows are marked on a plot of detecting efficiencies of different AFP stations vs. run numbers, which is identical to the figure 3.9.

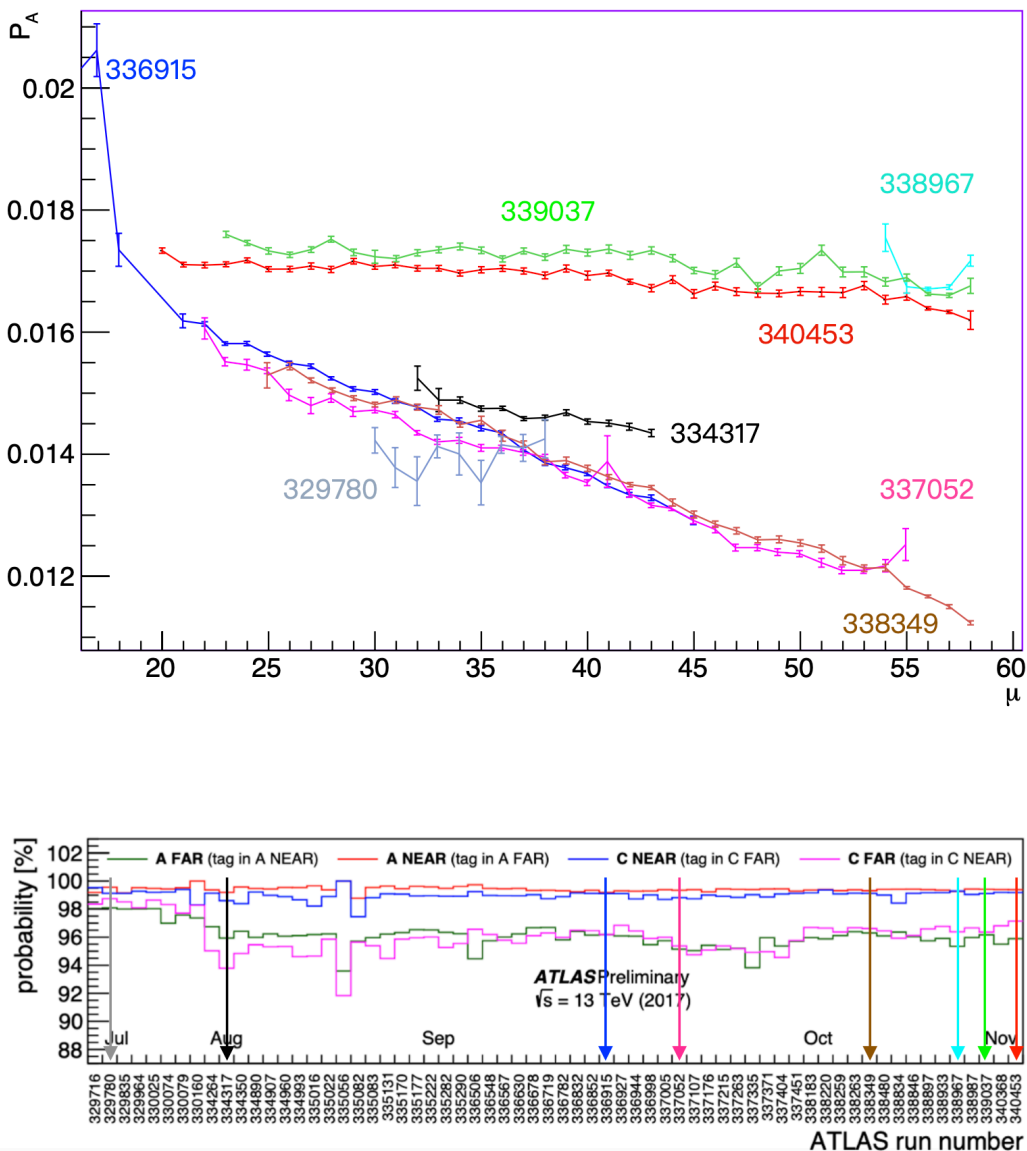


Figure 5.11: P_A calculated using data from different runs, drawn with respect to μ , together with the efficiencies of 4 AFP stations in different runs. The coloured arrows point out the time positions of the runs [37].

The difference between different runs in the probability results is large. Among all the sample runs we selected, some runs do show clear decreasing tendencies in the figure (for example, run 337052, run 336915, and run 338349), while some runs have significantly better consistency for different μ values (for example, run 339037 and run 340453). From the bottom plot of figure 5.11 we can conclude that the runs with relatively better consistency are mainly recorded in late 2017, while most of the earlier sample runs show evident gradients. This result indicates that the bad consistency of different runs is eligible to account for the tendency shown up on probabilities, and it is the most promising one among all of the three proposed possible causes. Similarly, figure 5.12 shows the P_C vs. μ and P_{AC} vs. μ curves for different runs, which shows that the inconsistency between different runs is valid for all of the three probabilities.

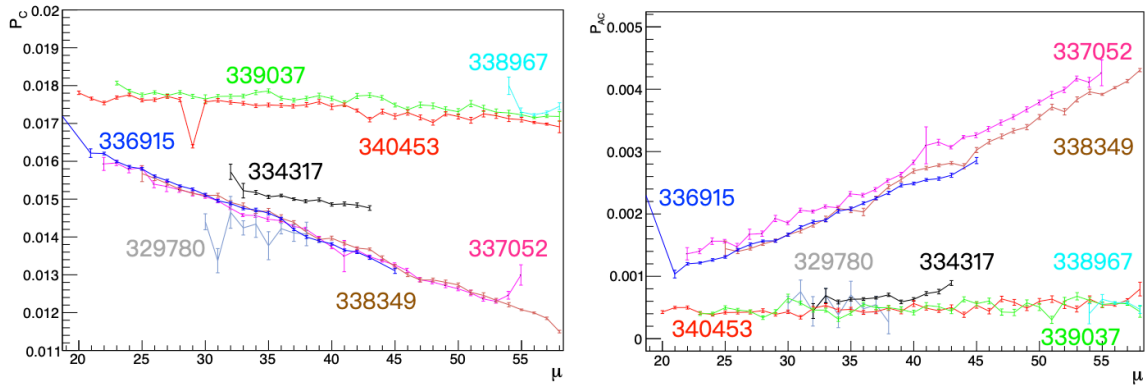


Figure 5.12: P_C and P_{AC} calculated using data from different runs, drawn with respect to μ . The definitions of different colors are consistent with that in figure 5.11.

However, since all the 55 runs used in the analysis have passed the GRL selection, all the runs involved should have good data qualities, and the different gradients in different runs are not expected.

Furthermore, according to the ATLAS trigger menu in 2017 [41], the only trigger menu applied in this analysis is the primary trigger menu, which is typically running unprescaled. Therefore, the most probable cause for the unexpected gradient is the trigger menu biases in different runs, which means, some trigger selections in the primary trigger menu in 2017 introduce run dependent biases to the data set. It is possible that these trigger selections are too harsh to the proton tracks in high pile-up events, resulting in the overestimation of the number of events with no proton detected

on each side of AFP, N_{00} , which leads to the negative gradient of the runs shown on the top plot of figure 5.11.

There are two methods that could be used to improve the results. One method is selecting the runs with small gradients on P_A vs. μ plots only, which is effective, but will lead to a sharp decline in the data amount.

The other method is using the minimum bias trigger menu instead of the primary trigger menu. The minimum bias triggers are a set of loosest selections from two approaches complementary in pseudo-rapidity: the Minimum Bias Trigger Scintillators (MBTS) that uses 16 scintillator counters on each side covering the pseudo-rapidity range of $2.09 < |\eta| < 3.84$, and the Inner Detector Minimum Bias triggers (ID Mb), which use Pixel and Semiconductor Trackers (SCT) covering the pseudo-rapidity range of $|\eta| < 2.5$ [46]. In MBTS triggers, at least one counter above threshold is required (L1_MBTS_1), and in ID Mb triggers, at least 3 SCT space points and 12 Pixel space points are required to reject empty events [46]. In all, these two methods are potential to improve the results, but such studies are left for future work.

In conclusion, using the data collected by AFP in 2017, the measured values for underlying probabilities are given by the overall average values:

$$\begin{aligned} P_A &= (14.0 \pm 0.001) \times 10^{-3}, \\ P_C &= (14.4 \pm 0.001) \times 10^{-3}, \\ P_{AC} &= (2.0 \pm 0.008) \times 10^{-4}, \\ P_0 &= (969.6 \pm 0.003) \times 10^{-3}. \end{aligned}$$

5.3 Conclusion

In this research, a probabilistic model based on predefined underlying probabilities is established. According to the data driven analysis shown in previous sections in

Chapter 5, the average values of underlying probabilities are measured to be:

$$\begin{aligned}
 P_A &= (14.0 \pm 0.001) \times 10^{-3}, \\
 P_C &= (14.4 \pm 0.001) \times 10^{-3}, \\
 P_{AC} &= (2.0 \pm 0.008) \times 10^{-4}, \\
 P_0 &= (969.6 \pm 0.003) \times 10^{-3}.
 \end{aligned}$$

According to the toy model simulation shown in Chapter 4, calculated underlying probabilities of the model should be constants with respect to various parameters. However, evident negative gradients are observed on $P_{A/C}$ vs. μ plots and positive gradients are observed on P_{AC} vs. μ plot, which has three potential causes: 1. the bias in μ calculation; 2. detector efficiency; 3. inconsistency of data in different runs. After the analysis, the third one is the most probable cause for the tendency, and it could be caused by the trigger menu biases in different runs. This can be tested by applying the minimum bias trigger menu instead of primary trigger menu. But this study is left for future work.

The performance analysis of AFP detector in 2017 is conducted. Based on the AFP data set in 2017, the distribution of average interaction number per bunch crossing, μ is presented, which consists of a continuum in the range $10 < \mu < 50$ and a peak at $\mu = 60$ produced by the luminosity leveling in 2017. Then the number of protons reconstructed on each side of AFP is presented, from which it can be concluded that the events with fewer than two protons on each side are the majority. The maximum detecting range of fractional momentum loss on A and C side, ξ_A and ξ_C are measured to be $0.025 < \xi_{A/C} < 0.12$. Finally, an "event mixing" method is applied to analyse the missing mass spectra. By comparing the missing mass distribution from normal events with that from normalised "mixed" events, it can be concluded that the line shape of pile-up backgrounds is consistent with the line shape of the missing mass distribution, indicating that the normal events are mainly made of pile-up background events.

References

- [1] D. M. Chew and G. F. Chew, "Prediction of double-pomeron cross sections from single-diffraction measurements," *Physics Letters B*, vol. 53, pp. 191–194, 1974.
- [2] R. Shankar, "Role of the pion mass in triple-regge physics," *Nuclear Physics B*, vol. 79, no. 1, pp. 126–140, 1974.
- [3] M. G. Albrow, "Double pomeron physics at the LHC," in *AIP Conference Proceedings*, AIP, 2005.
- [4] R. Lipes, G. Zweig, and W. Robertson, "Experimental consistency of multi-reggeism in a high-energy reaction," *Phys. Rev. Lett.*, vol. 22, pp. 433–437, 1969.
- [5] D. Denegri, J. Derre, M. Jabiol, S. Otwinowski, E. Pauli, P. Ermolov, E. Kistenev, A. Moiseev, M. Uchanov, H. Bialkowska, H. Blumenfeld, J. Loskiewicz, N. H. Khanh, E. Boos, and L. Sanko, "Double pomeron exchange and diffractive dissociation in the reaction $pp \rightarrow pp\pi^+\pi^-$ at 69 GeV/c," *Nuclear Physics B*, vol. 98, no. 2, pp. 189–203, 1975.
- [6] M. G. Albrow, "Double pomeron exchange: The early years," *AIP Conference Proceedings*, vol. 1654, no. 1, p. 040005, 2015.
- [7] M. Albrow, "Double pomeron exchange at the CERN intersecting storage rings and $sp\bar{p}s$ collider," *International Journal of Modern Physics A*, vol. 29, no. 28, p. 1446014, 2014.
- [8] M. Della Negra, D. Drijard, H. Fischer, G. Fontaine, H. Frehse, P. Frenkiel, C. Chesquiere, R. Gokieli, P. Hanke, W. Hofmann, W. Isenbeck, E. Kluge, V. Korbel, D. Linglin, A. Minten, A. Norton, A. Putzer, R. Sosnowski, S. Stein, and D. Wegener, "Study of double pomeron exchange in pp collisions at $\sqrt{s}=31$ GeV," *Physics Letters B*, vol. 65, no. 4, pp. 394–396, 1976.
- [9] M. Albrow, "Central exclusive production at the Tevatron," *International Journal*

- of Modern Physics A*, vol. 29, no. 28, p. 1446009, 2014.
- [10] Particle Data Group, “Review of Particle Physics,” *Progress of Theoretical and Experimental Physics*, vol. 2022, no. 8, 2022.
- [11] S. L. Glashow, “Partial-symmetries of weak interactions,” *Nuclear Physics*, vol. 22, no. 4, pp. 579–588, 1961.
- [12] S. Weinberg, “A model of leptons,” *Phys. Rev. Lett.*, vol. 19, pp. 1264–1266, 1967.
- [13] A. Salam, *Weak and electromagnetic interactions*, pp. 244–254. World Scientific, 1994.
- [14] J. Lorenzo Diaz-Cruz, “The higgs profile in the standard model and beyond,” *Revista Mexicana de Fisica*, vol. 65, no. 5, pp. 419–439, 2019.
- [15] F. Englert and R. Brout, “Broken symmetry and the mass of gauge vector mesons,” *Phys. Rev. Lett.*, vol. 13, pp. 321–323, 1964.
- [16] P. W. Higgs, “Broken symmetries and the masses of gauge bosons,” *Phys. Rev. Lett.*, vol. 13, pp. 508–509, 1964.
- [17] S. M. Bilenky, “Neutrinos: A brief review,” *Modern Physics Letters A*, vol. 19, no. 33, pp. 2451–2477, 2004.
- [18] P. Wang, “Color confinement, dark matter and the missing anti-matter,” *Journal of Physics G: Nuclear and Particle Physics*, vol. 48, p. 105002, sep 2021.
- [19] L. Adamczyk, E. Bana, A. Brandt, M. Bruschi, S. Grinstein, J. Lange, M. Rijssenbeek, P. Sicho, R. Staszewski, T. Sykora, M. Trzebiski, J. Chwastowski, and K. Korcyl, “Technical Design Report for the ATLAS Forward Proton Detector,” tech. rep., CERN: CERN-LHCC-2015-009, reportNumber =.
- [20] ATLAS Collaboration, “ATLAS: Detector and physics performance technical design report. Volume 2,” *ATLAS Technical Reports*, 1999.
- [21] ATLAS Collaboration, “Measurement of differential cross sections for single diffractive dissociation in $\sqrt{s} = 8$ TeV pp collisions using the ATLAS ALFA spectrometer,” *JHEP*, vol. 02, p. 042, 2020.
- [22] K. Goulianos, “Diffractive interactions of hadrons at high energies,” *Physics Reports*, vol. 101, no. 3, pp. 169–219, 1983.
- [23] D. Roy and R. Roberts, “Triple-regge analysis of $pp \rightarrow px$ and some related phe-

- nomena a detailed study," *Nuclear Physics B*, vol. 77, no. 2, pp. 240–268, 1974.
- [24] A. M. Mueller, "o(2, 1) analysis of single-particle spectra at high energy," *Phys. Rev. D*, vol. 2, pp. 2963–2968, Dec 1970.
- [25] M. Trzebiński, "Diffractive physics at the LHC," *Ukrainian Journal of Physics*, vol. 64, p. 772, sep 2019.
- [26] TOTEM Collaboration, "First measurement of elastic, inelastic and total cross-section at $\sqrt{s} = 13$ TeV by totem and overview of cross-section data at LHC energies," 2019.
- [27] ATLAS Collaboration, "Observation and measurement of forward proton scattering in association with lepton pairs produced via the photon fusion mechanism at ATLAS," tech. rep., CERN: ATLAS-CONF-2020-041, Geneva, 2020.
- [28] J. Jaeckel, G. Rybka, and L. Winslow, "Snowmass 2021 white paper: Axion dark matter," Proceedings of the US Community Study on the Future of Particle Physics (Snowmass 2021).
- [29] J. Wenninger, "The LHC collider," *Comptes Rendus Physique*, vol. 16, no. 4, pp. 347–355, 2015.
- [30] L. R. Evans, *The Large Hadron Collider: a marvel of technology*. EPFL Press, 2009.
- [31] F. Bordry, "Status of the Large Hadron Collider (LHC)," *LHC Project Report 1130*, p. 6 p, 2008.
- [32] O. S. Brüning, P. Collier, P. Lebrun, S. Myers, R. Ostojic, J. Poole, and P. Proudlock, *LHC Design Report*. CERN Yellow Reports: Monographs, Geneva: CERN, 2004.
- [33] ATLAS Collaboration, *ATLAS: technical proposal for a general-purpose pp experiment at the Large Hadron Collider at CERN*. LHC technical proposal, Geneva: CERN, 1994.
- [34] L. Evans and P. Bryant, "LHC machine," *Journal of Instrumentation*, vol. 3, no. 08, pp. S08001–S08001, 2008.
- [35] ATLAS Collaboration, "The ATLAS experiment at the CERN large hadron collider," *Journal of Instrumentation*, vol. 3, no. 08, pp. S08003–S08003, 2008.
- [36] ATLAS Collaboration, *ATLAS pixel detector: Technical Design Report*. ATLAS Report, Geneva: CERN, 1998.

- [37] S. Grinstein, "The ATLAS forward proton detector (AFP)," *Nuclear and Particle Physics Proceedings*, vol. 273-275, pp. 1180–1184, 04 2016.
- [38] ATLAS Collaboration, "Performance of the ATLAS forward proton spectrometer during high luminosity 2017 data taking," *ATLAS Note*, no. ANA-FDET-2019-04-INT1, 2020.
- [39] M. Oriunno, M. Deile, K. Eggert, J.-M. Lacroix, S. J. Mathot, E. P. Noschis, R. Perret, E. Radermacher, and G. Ruggiero, "The Roman Pot for LHC," p. 562. 3 p, 2006.
- [40] M. G. Albrow, H. Kim, S. Los, M. Mazzillo, E. Ramberg, A. Ronzhin, V. Samoylenko, H. Wenzel, and A. Zatserklyaniy, "Quartz cherenkov counters for fast timing: QUARTIC," *Journal of Instrumentation*, vol. 7, no. 10, p. 10027, 2012.
- [41] ATLAS Collaboration, "Trigger Menu in 2017," tech. rep., CERN: ATL-DAQ-PUB-2018-002, Geneva, 2018.
- [42] ATLAS Collaboration, "ATLAS data quality operations and performance for 2015–2018 data-taking," *Journal of Instrumentation*, vol. 15, no. 04, pp. P04003–P04003, 2020.
- [43] C. M. S.-M. E. M. T. Bray, J. Paoli and F. Yergeau, "Extensible markup language (xml) 1.0," *W3C recommendation*, no. fifth edition, 2008.
- [44] M. Kocian, "Readout and trigger for the afp detector at atlas experiment," *Journal of Instrumentation*, vol. 12, 1 2017.
- [45] B. Muratori and T. Pieloni, "Luminosity levelling techniques for the LHC," *ICFA Mini-Workshop on Beam-Beam Effects in Hadron Colliders*, pp. 177–181, 2014.
- [46] R. Kwee, "Minimum bias triggers at ATLAS, LHC," 34th International Conference on High Energy Physics, Philadelphia, 2008.